Coupling the Radial Vibrational Modes of Mixed Barium-Ytterbium Chains for Quantum Computing

Tomasz Sakrejda

A dissertation
submitted in partial fulfillment of the
requirements for the degree of

Doctor of Philosophy

University of Washington

2017

Reading Committee:

Boris Blinov, Chair

Subhadeep Gupta

Xiaodong Xu

Program Authorized to Offer Degree:
Department of Physics

University of Washington

Abstract

Coupling the Radial Vibrational Modes of Mixed Barium-Ytterbium Chains for Quantum Computing

Tomasz Sakrejda

Chair of the Supervisory Committee:
Associate Professor Boris Blinov
Department of Physics

The advantages of mixed species ion chains may be essential to scaling a quantum computer; however, using them requires a better understanding of mixed species ion trapping and manipulation than we currently posses. In this thesis I perform measurements of the efficiency of sympathetic cooling of mixed barium-ytterbium ion chains. After initially measuring temperatures, I investigate the vibrational mode couplings. I discover parameters for a linear Paul trap for which 2-Ba-2-Yb chains are cooled to near the Doppler limit, and for which their vibrational modes are coupled well enough to perform entangling gates. I find numerically that these parameters should scale well to at least ten ions. Instabilities of the trap and of the 1762 nm 'shelving' laser system are systematics on my measurements, so I also characterize various noise sources related to the experiment.

TABLE OF CONTENTS

LIST OF FIGURES

LIST OF TABLES

ABBREVIATIONS

ADC Analog to Digital Converter. Converts analog voltage or current signals to the digital representation of a corresponding number in Volts or Amperes.

AOM Acousto-Optic Modulator. Device to diffract an incoming laser beam against a rf standing wave. Allows the frequency and power of a diffracted beam to be quickly controlled by changing RF parameters.

CCD Charge coupled display. A camera sensor

CW Continuous Wave. Mode of laser operation with constant light emission. Often used to distinguish from pulsed or mode-locked operation, where the laser outputs light in discrete pulses.

DAC Digital to Analog Converter. Converts a digital representation of a number to a corresponding analog signal of that many Volts or Amperes.

DC Direct Current. Current flowing in a constant direction. Often used to refer to signals with no time variation.

DPAOM Double Passed Acousto-Optic Modulator. Optical system that diffracts light twice off an AOM to increase optical isolation and minimize pointing shifts due to changing the rf frequency applied to the AOM.

ECDL External Cavity Diode Laser. Laser made by externally frequency selecting and feeding back light into a laser diode.

EMCCD Electron Multiplying Charge Coupled Device. Charge coupled device with an electron multiplying readout channel with controllable gain.

EOM Electro-Optic Modulator. Device to modulate a laser beam with an electric control field. Allows modulation of the frequency, power, or phase of the beam.

FWHM Full Width at Half Maximum. Distance between half maximum points on a peak.

HWHM Half Width at Half Maximum. Distance between half maximum and center of a peak.

HWP Half Wave Plate. Delays light polarized along one direction by half a wavelength while not affecting the orthogonal direction of polarization. Often used to rotate the polarization of light by a desired angle.

NA Numerical Aperture. A number that characterizes the range of angles over which the system can accept or emit light.

OSLO Optics Software for Layout and Optimization. Optics simulation software.

PBS Polarizing Beam Splitter. Reflects light polarized along one direction while transmitting the orthogonal direction of polarization.

PID Controller Proportional, Integral, Differential Controller. Feedback controller with three feedback terms proportional to the error signal, its integral, and its derivative.

PMT Photomultiplier Tube. Single photon detection device based on photoelectron amplification.

PPLN Periodically Poled Lithium Niobate. Type of crystal used in frequency conversion applications.

QWP Quarter Wave Plate. Delays light polarized along one direction by a quarter of a wavelength while not affecting the orthogonal direction of polarization. Often used to elliptically or circularly polarize light.

RF Radio Frequency. Frequencies between a few kHz and $\approx$ 1000 GHz.

SNR Signal-to-noise ratio

UHV Ultra-High Vacuum. Pressures below 10^{-9} torr. Usually only achievable with all metal seals and careful chamber preparation.

ACKNOWLEDGMENTS

This thesis builds on the work of many previous graduate students. I enjoyed working with John Wright and testing his patience as I destroyed various pieces of equipment during my early days in the lab. He offered many helpful pieces of experimental and practical advice, only some of which necessitated the smell of burning electronics. Tom Noel, Matt Hoffman, and Carolyn Auchter all offered advice and commiserated as only ion trappers can. It was also great to work with Spencer Williams, whose sense of humour livened the lab, and whose openness led to many useful discussions over the years. I would also like to thank the newer generation of students for their contributions and for their patience as I learned to be a better teacher. Jennifer Lilieholm, Liudmila Zhukas, Mike Clancy, Justin Burau, Wen-Lin Tan, and Matt Bohman all did great work and it has been my pleasure to work with them.

I would like to thank my parents, who helped to nurture my appreciation of science and supported me throughout my academic career. Visits to my mother's work at Lawrence Berkeley National Laboratory helped spark my interest in Physics, and my dad always had my back whenever I got myself into trouble. I am deeply grateful for their support throughout the years. I would also like to thank both of my brothers for not throwing me over a cliff/into a boiling hotspring when I was younger, and for supporting me now.

My advisor Boris Blinov has been an inspiration throughout my time at UW. His inventiveness and the depth of his understanding helped break through many technical difficulties. I am also profoundly grateful for his unwavering support- Boris has always been willing to go to bat for a students' good idea, and has made his appreciation for the work of those under him clear. He also inadverntently helped teach me a painful lesson in time management with the creation of this thesis, which I hope to remember for a long while. On that note, I would like to thank Akshay Ghalsasi and Jennifer Lilieholm for their help in editing this

thesis- I would never have made the deadline without them. I would especially like to thank Mackenzie Barton-Rowledge, who helped edit this thesis, brought food as I scrambled to finish it, and prodded me to get the administrative drudgery done.

I also want to thank a few people who helped in less direct ways. Dr. Rosellini found a a treatment for my migraines that made both work and life infinitely more pleasant. Without it I honestly don't know if I could have finished my work here. I would also like to thank those who listened to my complaints about technical problems and responded with advice and encouragement. There are too many to list by name because of the vigorousness of my complaining, but I would like to thank Isaac, John, Durmus, and Julieta especially for giving technical feedback that I ended up implementing. I've been glad to be kept company by my old friends Sarah, Paul, and Michael, and fresher faces Derek, Stella, Laura, Matthias, Akshay, Keoni, and Sara. I would also like to thank April and Jamie for reminding me that I should try to actually have fun once in a while.

Chapter 1

INTRODUCTION

1.1 Quantum Computing

Quantum computing has the potential to make new classes of problems solvable[1], and so is of great interest to both the scientific and computer science communities. For example, it is currently impossible to simulate large highly entangled quantum mechanical systems for any reasonable time, as classical algorithms require exponential resources in space, time, or processing power to produce the true quantum mechanical solution. Difficult as it is to classically simulate large quantum mechanical systems, finding the solution using qubits (the quantum version of bits) is also non-trivial. Attempting to precisely and completely control a fully quantum mechanical system with even a few degrees of freedom has taken decades. A prosaic saying in the quantum computing community is, "You can have qubits that work or you can have qubits that scale. Qubits that scale don't work, and qubits that work don't scale."

Many groups of academics are working with different quantum systems which could be used for a universal quantum computing framework. These include trapped ions[2], quantum dots[3], superconducting junctions[4], neutral atoms [5], and photons[6]. Different paradigms for quantum computing exist inlcuding adiabatic[7] & measurement based quantum computing[8], but I will restrict my attention to the most fully realized "gate circuit model". On a practical level, only superconducting qubits[9] and trapped ions[10] have achieved the minimum entangling gate fidelity necessary for extended quantum computation[11][12], where fidelity is defined as the overlap between a target quantum state and the actual state after the gate. Scaling high fidelity gates to large numbers of qubits is currently the greatest challenge in this field.

Recent efforts by Google, IBM, and IonQ suggest that we may be on the cusp of solving some of the scaling problems in quantum computing. In 2016 IBM provided a pub-

lic interface on the internet for a small quantum computer. It has five superconducting qubits, achieves a 96.5% two qubit gate fidelity, and is being used for quantum information research[13][14]. Google has built a nine qubit machine which they have used to simulate a hydrogen molecule[15] and they have announced plans to build a 50 qubit machine by the end of 2017. Superconducting quantum computers still require optimization, fine tuning, and expensive equipment, but these barriers are falling[16]. Ion trap quantum computers are also becoming a reality; in 2017 IonQ built a fully-connected five qubit ion trap quantum computer with 96.8% two qubit gate fidelity[17]. As no clearly superior physical system or logical architecture has yet emerged, it is worthwhile to continue to improve different quantum information technologies. This thesis investigates aspects of the physical implementation of a trapped ion quantum processor, and more specifically those operations which are performed inside of a single ion trap.

In 2000 David P. DiVincenzo published a paper spelling out the physical requirements for the implementation of a universal quantum computer[18]. There are five criteria in total. The first is a scalable physical system with well characterized qubits. We need to be able to create a system consisting of however many qubits we require in order to build a scalable computer. The qubits must also be fully understood, so that we can manipulate their physical dynamics, and so that we can successfully interpret measurements of the qubits. The second criterion states that we must be able to initialize all qubits into a simple known state with very high fidelity. This arises both from a computing requirement that our logical registers are set to a known state before computation, and from quantum error correction's need for qubits prepared with low entropy. The third criteria is that our qubits must interact weakly enough with the environment to maintain their superpositions and entanglement for a relatively long time. Stated differently, the qubits must have a "coherence time" at least long enough to implement error correction so that we can perform larger computations. The fourth requirement is a "universal" set of quantum gates. The Solovay-Kitaev theorem guarantees that given a set of a few simple one or two qubits gates satisfying some requirements, we can approximate an arbitray unitary transformation. These gates need to happen quickly with respect to the decoherence time of our quantum system, so that we may chain many of them together. Finally, we need the ability to measure

the results of our qubits individually. If we can only gain information about the average distribution of our quantum system after its computation we will not have access to the qubit-specific correlations which enhance the performance of quantum computers. All of these criteria are fulfilled in the implementation of ion trap quantum processors.

1.2 Quantum Computing in Ion Traps

The Modular Universal Scalable Ion-trap Quantum Compuiter (MUSQIC) architecture[19] depicted in schematic form in figure 1.1, forms the basis of our group's work towards trapped ion quantum computing. Many ions with hydrogen-like energy levels are trapped together in "quantum registers", and the ions' ground or metastable states are used as qubit levels. Traditional ion traps are bulky and a powerful quantum computers would require large amount of space. To mitigate this problem, miniaturized trap designs which use semiconductor processing techniques reduce the footprint of each quantum register. These miniaturized traps have hundreds of control electrodes which can be used to manipulate the ions. The electrodes can change the static trapping potential, separate ions in a single trap, and shuttle ions around the trap. Ions inside a single trap can be manipulated in different ways. Microwaves and RF fields drive can drive global qubit rotations[20] or even single qubit gates[21], and laser beams drive single qubit gates, or multi qubit gates by coupling the ions' internal levels to the collective vibrations of the coulomb crystal[22][10].

A single trap can only hold so many ions in a linear chain. For this reason trapped ion quantum computers require interconnects between traps in order to scale past $\sim$100 ions[19]. In the MUSIQC architecture, entanglement between different traps, termed remote entanglement, is carried as follows. Specific trapped ions in the chain are reserved for creating photonic interconnects. Pulsed, resonant excitation probabilistically entangles the atomic state with a photon emitted after spontaneous decay. Photons from two separate ions are then interfered on a beam splitter and the outputs are fed into polarization analyzers. A simultaneous click on two photon counters heralds the creation of a Bell state between the ions which emitted the photons[23]. If no entanglement is created after such a pulse sequence, the procedure is simply repeated until a heralded entanglement is achieved. Commerical optical multiplexers are available which could arbitrarily switch the beampath

between different traps, allowing remote entanglement to be carried out between any pair of traps. Using this procedure entanglement fidelities of 90% have been achieved in ion traps. Remote entanglement fidelities remain fairly low, but there are workable improvements, including better collection optics and better photon mode matching[24].

The MUSIQC architecture also includes the possibility of using mixed species ion chains in the quantum registers. Using mixed species allows one to choose the best properties of different ions to exploit for particular tasks, but more importantly it allows one to change the atomic state of one set of ions without disrupting the other. One set can then be "logical" ions which store quantum information, while the other are "utility" ions used for other tasks. In the MUSIQC architecture, $^{171}Yb^{+}$ are logic ions, while $^{138}Ba^{+}$are utility ions. Two applications are clearly useful. The first is sympathetic cooling, in which the utitlity ions are laser cooled while the logical ions are used for quantum information operations. The cooled ions act as refrigerants, periodically extracting heat from the system, but the quantum information stored in the logical ions is not disrupted. The second is remote entanglement. To create a remote entanglement it is necessary to apply resonant light to the at least one ion in the trap, and any crosstalk of the excitation beam with neighboring ions could disrupt their quantum states. Currently the sucess rate for remote entanglement is very low, so it must be repeated many times, and the likelihood of crosstalk is compounded. In MUSIQC, instead of entangling logical ions, remote entanglement is done with utility ions, and the entanglement is swapped using local gates onto the logical ions.

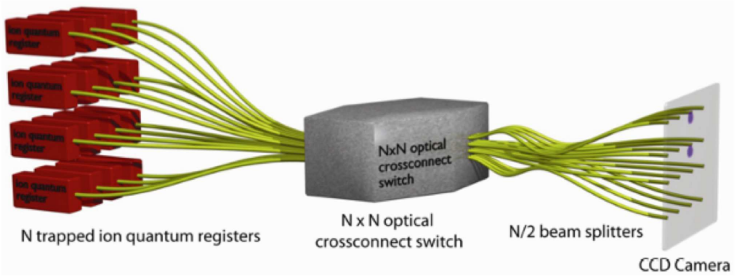

Figure 1.1: Schematic of the MUSIQC architecture. Quantum registers holding hundreds of trapped ion qubits perform parts of the computation and error correction. Specific ions within these registers are used for remote entanglement, and are repeatedly excited with pulsed resonant light. The emitted photons, entangled with the atomic states, are multiplexed with an optical crossconnect switch, interfered on beam splitters, and detected with a CCD camera.

Chapter 2

RELEVANT TECHNIQUES

2.1 Paul Traps

The eponymous tool of ion trapping merits brief discussion. An ion trap consists of a configuration of fields which can confine a charged particle (ion) to a defined, and in many cases nearly empty, region of space. Naively one might consider confining the ion electrostatically, however Laplace's equation does not allow for a potential well to exist in free space. Instead of using an entirely electrostatic confining potential we must apply either time-varying electric fields or magnetic fields, as in Paul traps or Penning traps respectively. I will mention Penning traps only briefly, as they are not used in this work. Penning traps are cylindrically symmetric, with a strong magnetic field that confines the ions in the radial direction, and a static potential providing confinement along the axis. A typical cold trapped ion crystal confined in such a trap will rotate at frequencies between a few and many hundreds of kHz[25]. In a quantum information platform the rotation complicates state readout and quantum logic operations, so most quantum information efforts in trapped ions are carried out in Paul traps. Recently, however, there has been interest in simulating two and three dimensional quantum systems using crystals in these types of traps, and the first experiments with some hundreds of ions have been performed[26].

Paul traps instead confine ions using a time-varying quadrupole electric field. In the early days of ion trapping experimentalists put a large amount of effort into machining hyperbolic electrodes which would produce a perfectly quadrupolar field. It was quickly realized that such effort was wasted, as a wide variety of electrodes produce an acceptably quadrupolar potential[27]. An ion trap acceptable for some purposes in modern apparatuses can be produced today simply by twisting wire to form a ring. We use a linear Paul trap, schematically shown in 2.1 because it allows us to place many ions at the null of the time-varying potential, which reduces frequency modulation and heating. Two end-cap electrodes

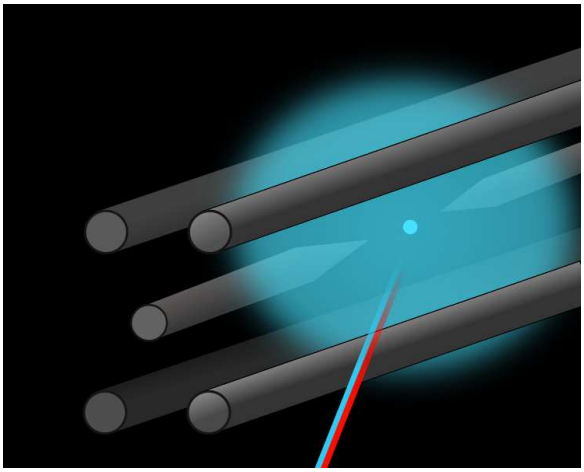

Figure 2.1: A cartoon of a linear four-rod Paul Trap containing a single Ba^+ fluorescing under resonant excitation with 493 nm(cyan) Doppler cooling and 650 nm(red) repump lasers. Static potentials are applied to the two needles along the trap axis which push the ion towards the trap center. Two rods on opposite corners are grounded, while the other two have an applied oscillating potential. The effect of this potential, on time average, is to create a harmonic trap for the ion in the radial direction.

on the axis are held at voltage V_static, creating a potential at the center of the trap

$$\Phi_{axial} = \kappa V_{\text{static}} \left[z^2 - \frac{1}{2}(x^2 + y^2) \right], \tag{2.1}$$

where z is the direction along the trap axis, x and y are the orthogonal "radial" directions, and κ is a geometric factor related to the trap shape. Four trap rods stretch along the z axis, spaced away from the trap center at $\pm R\hat{x}, \pm R\hat{y}$. They do not contribute to the axial potential, as they are translationally invariant in that direction. The motion of a charge q of mass m along the trap axis is determined by the z^2 term and is therefore harmonic, with frequency $\Omega_z = \sqrt{2\kappa q V_0/m}$. Two of the rods are grounded, and an oscillating voltage is applied to the other two. The radial potential, including end-cap and rod terms, is then

$$\Phi_0 = (U_{RF}\cos(\Omega_T t) + U_{squeeze}) \left[1 + \frac{x^2 - y^2}{2R^2} \right] - \kappa V_{\text{static}}[-\frac{1}{2}(x^2 + y^2)], \tag{2.2}$$

where U_{RF} is the amplitude of the oscillating voltage, Ω_T is the applied frequency, t is time, and $U_{squeeze}$ is the static component of the oscillating voltage. The radial equations of motion for $u_i = x, y$ can be rescaled and cast in the form of the Mathieu equation,

$$\frac{d^2 u_i}{d\xi^2} + (a_i + 2q_i\cos(2\xi))u_i = 0 \tag{2.3}$$

$$\xi = \Omega_{\text{T}} t/2 \tag{2.4}$$

$$a_i = -\frac{4q}{m\Omega_T^2}(\kappa U_{static} \mp \frac{U_{squeeze}}{R^2}) \tag{2.5}$$

$$q_i = \pm\frac{2qU_{\text{rf}}}{\Omega_{\text{T}}^2 m R^2}. \tag{2.6}$$

The Mathieu equation can be solved in general using the Floquet solutions. We restrict ourselves to the region where ion traps typically operate, $a_i \ll q_i \ll 1$. The equations of motion can be written as

$$u_i(t) = A_i\cos(\omega_i t + \phi_i)\left(1 + \frac{q_i}{2}\cos(\Omega_{\text{T}} t)\right), \tag{2.7}$$

where A_i and ϕ_i depend on initial conditions, q_i is defined as above, t is time, and ω_i is

$$\omega_i \equiv \frac{\Omega_{\text{T}}}{2}\sqrt{a_i + \frac{q_i^2}{2}}. \tag{2.8}$$

The oscillation at frequency ω_i is called the secular motion of the ion. For small excursions from the trap center the ion experiences a perfect harmonic oscillator potential which may

be quantized as usual. The oscillation at the trap frequency Ω_T is called micromotion and corresponds to the driven motion of the ion by the applied electric field. It becomes larger if there is any electric field in the radial direction pushing the ion away from the trap null. Micromotion can modulate laser frequencies in the ion rest frame via the Doppler shifts, so care must be taken to ensure that it does not ruin the efficiency of cooling or interfere with coherent operations.

2.2 Doppler Cooling

2.2.1 Theory

When first trapped, the ions are literally hot out of the oven. They're moving a few hundred m/s, and are making excursions from our trap center of approximately 250 μm. Their transitions are significantly Doppler shifted and they experience nonuniform laser intensities, which makes quantum operations difficult. In the MUSIQC architecture we use a method termed "Doppler" cooling to slow the ions down. A laser addresses a strong transition with a slight negative detuning. This allows our ions to preferentially absorb photons when it slows them down: the Doppler shift in the frequency due to the movement of the ions makes the difference between being on resonance – and the ion absorbing many photons coming from only the direction opposite to its movement – or not. The emission is isotropic and contributes no net momentum to the ions. Here for simplicity we consider a two level ion with motion in only one dimension, and ignore the quantum mechanical nature of the ions' motion in the trap. These approximations do not change the most important features of the result.

The time-average force from continuous scattering of photons by the ion can be found to be

$$F_{scatter} = \hbar k \frac{\Gamma}{2} \frac{s}{1 + s + \frac{4\delta^2}{\Gamma^2}}, \tag{2.9}$$

,where Γ is the atomic transition linewidth, $s \equiv \frac{2\Omega^2}{\Gamma^2}$ is the saturation parameter. Ω is the Rabi frequency, $k = 2\pi/\lambda$ is the laser's wavenumber, and δ is the frequency detuning between the laser and the center of the atomic transition. By averaging we are ignoring fluctuations in this scattering force due to inherent randomness of absorption and emission.

The static effect of the scattering force is a shift of the equilbrium position in our harmonic trap, which is approximately 10 nm. This spatial shift is small compared to the ion spacing, and corresponds to an energy small compared to the energy level spacings of the trap. The second effect is due to the Doppler shift: as the ion executes its motion inside the harmonic trap, the laser frequency is modulated by the Doppler effect so that for nonrelativsitic velocities, $\delta \to \delta - kv$, where v is the velocity of the ion in the direction of the laser beams. For Doppler shifts small compared to the linewidth, the force on the ion becomes

$$F_{Doppler} = F_{scatter}(\delta - kv) - F_{trap} \tag{2.10}$$

$$F_{Doppler} \simeq -\frac{\partial F_{scatter}}{\partial \delta} kv \tag{2.11}$$

$$F_{Doppler} = F_{scatter}\left(\frac{8k\delta/\Gamma^2}{1 + s + \frac{4\delta^2}{\Gamma^2}} v\right). \tag{2.12}$$

As the Doppler force is proportional to the velocity, for negative detunings our applied laser provides a damping force on the ion's motion. Presently we would expect that the ion's velocity should approach zero, however those fluctuations and random emissions we ignored because of the time average limit us to a nonzero speed. The recoils lead to a random walk in the ion velocity, which means that the mean square ion velocity increases by $(\hbar k/m)^2 R_{scatter} t$ in a time t where $R_{scatter}$ is the scattering rate. Equating this heating process with the cooling due to the damping force, we find an equilibrium mean square velocity

$$\bar{v}^2 = \hbar \frac{\Gamma^2}{4m\delta}(1 + s + \frac{4\delta^2}{\Gamma^2}), \tag{2.13}$$

where m is the barium mass. Optimizing the saturation s and detuning δ to achieve the minimum kinetic energy we find

$$m\bar{v}^2 = \hbar \frac{2\Gamma}{m}. \tag{2.14}$$

Despite the fact that much of the work in quantum information involves only a few ions, temperature is often used as a shorthand to describe kinetic energies. Finding the associated temperature through the equipartition theorem we find $T_{Doppler} = 2\hbar\Gamma/k_b$, where k_b is the boltzmann constant. For Ba^+, this temperature is 1.5 mK.

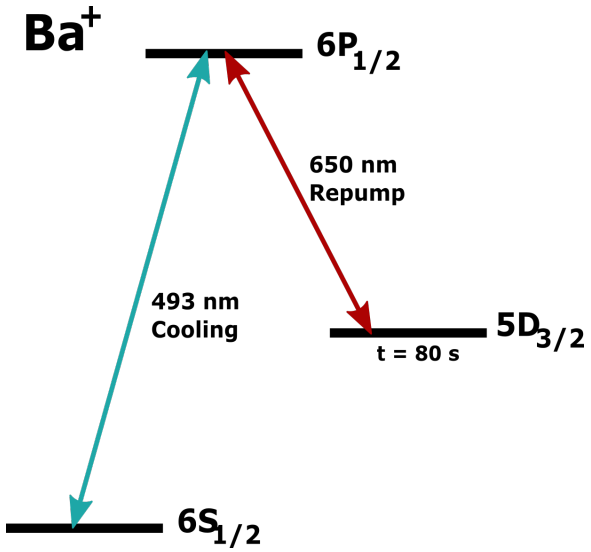

Figure 2.2: A schematic of the optical transitions and atomic structure of $^{138}Ba^{+}$relevant to Doppler cooling and state initialization. Again a magnetic field is applied which lifts the degeneracy of the Zeeman levels, but only some of the sublevels are shown.

2.2.2 Reality

Because Barium can decay to a long-lived metastable state during its cooling process, we must use a second laser during Doppler cooling to keep the ions interacting with the cooling laser, see fig 2.2 . Specifically, the main cooling laser at 493 nm excites the ion to the $6P_{1/2}$ state. While the ion is most likely ($\approx 75\%$) to decay from there to the $6S_{1/2}$ ground state, where it can continue cooling by absorbing 493 nm photons, it can also decay to the $5D_{3/2}$ state 25% of the time. The $5D_{3/2}$ state has a lifetime of $\sim$80 s [28], unless a 650 nm laser is used to drive a transition from the $5D_{3/2}$ state back to the excited $6P_{1/2}$ state where it can rejoin the cooling cycle. The existence of this laser and decay pathway introduces an additional laser force, decreases the 493 nm scattering rate, and introduces a two-photon coupling between $6S_{1/2}$ and $5D_{3/2}$. Because of Ba^{+}'s large branching ratio to $5D_{3/2}$, the strength of all of these effects is large. The two-photon coupling causes the greatest difficulties experimentally because cooling efficacy becomes a sensitive function of both laser powers and their frequencies[29]. This effect can be seen in my diagnostic

measurements: in section 4.1 I measure a single trapped ion to have a temperature 20x the Doppler limit despite employing reasonable cooling parameters. Numerical studies and previous temperature measurements place the full three-level limit at about a few times the standard Doppler limit.

2.3 State Initialization

Efficient state preparation is necessary both for barium and ytterbium ions in the MUSIQC architecture. The initialization scheme for $^{138}Ba^{+}$is shown in figure 2.3. We use a nuclear-spin zero isotope of barium, so we apply a homogenous, static magnetic field in order to lift the degeneracy of the two ground state Zeeman levels. We optically pump the ion preferentially to one of the two Zeeman levels by coupling all other available states to one which decays to our desired state. σ^{+} 493 nm light sent in along the quantization axis couples $m_s = -1/2$ state to $6P_{1/2}$ but not $m_s = +1/2$ due to angular momentum conservation. If the ion decays to $5D_{3/2}$, the 650 nm repumps it to $6P_{1/2}$, evacuating the $5D_{3/2}$ levels. After a few optical cycles the ion is pumped into the $m_s = +1/2$ state.

As $^{171}Yb^{+}$ has a cycling transition and a large hyperfine splitting, state preparation does not require polarization discrimination. The state initialization scheme is shown in figure 2.3. The $S_{1/2}$ $F = 1$ states are coupled to the $P_{1/2}$ $F = 1$ excited state with a 369 nm laser. The P state decays to either the $S_{1/2}$ $F = 0$ ground state or to the metastable $D_{3/2}$ levels. Both of the $D_{3/2}$ manifolds are repumped to $D[3/2]_{1/2}$ with a laser at 935 nm, from which they decay back to the ground state.

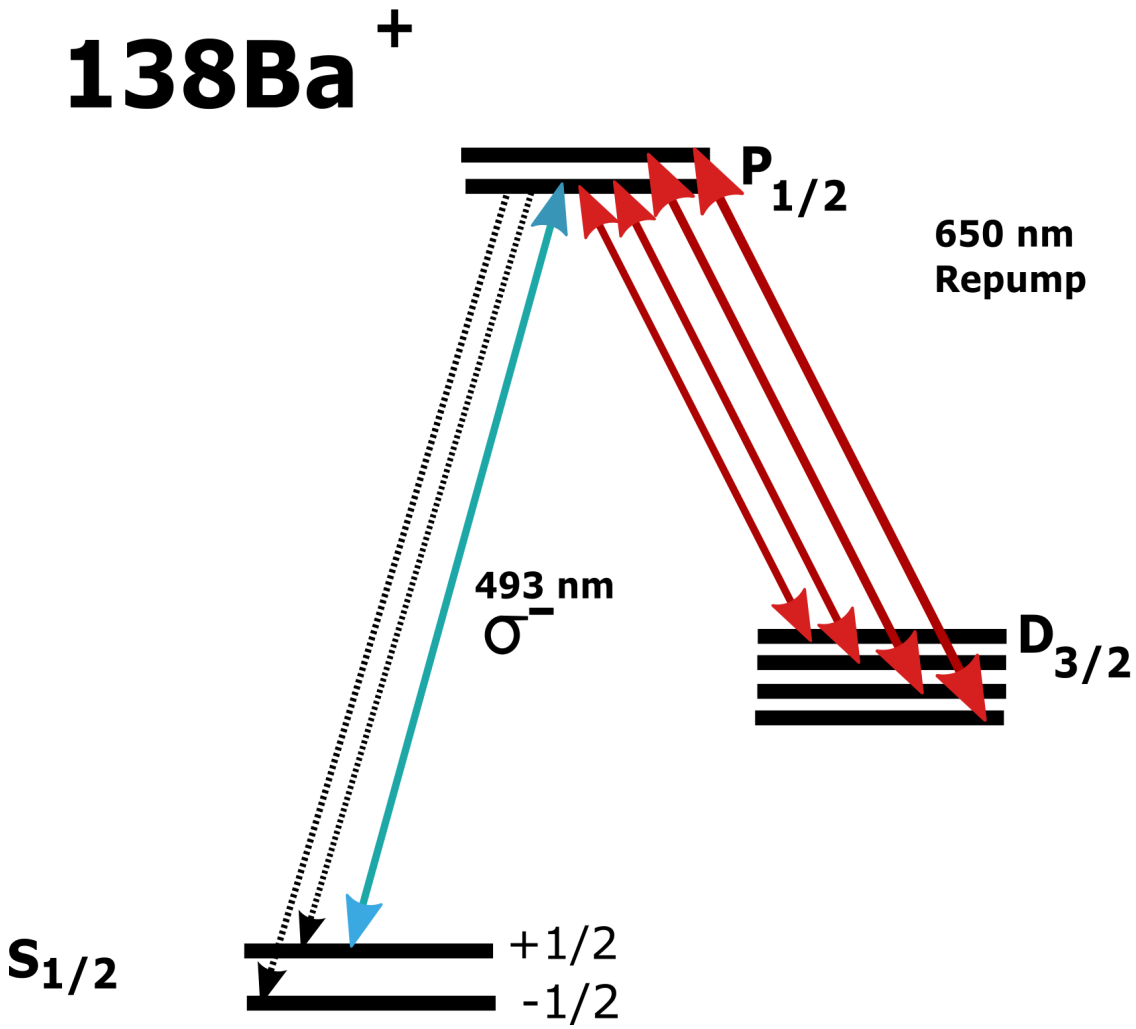

Figure 2.3: A schematic of the optical transitions and atomic structure of $^{138}Ba^{+}$relevant to state initialization. An applied magnetic field lifts the degeneracy of the Zeeman levels. Dashed lines represent spontaneous decays, while solid lines indicate driven transitions.

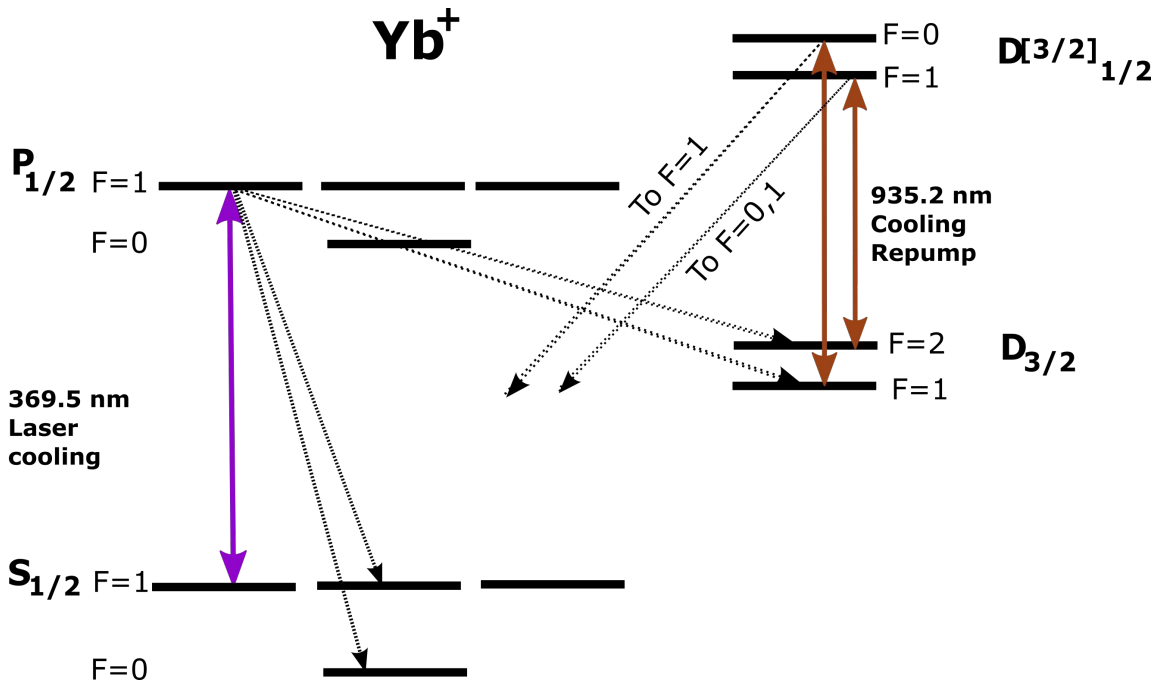

Figure 2.4: A schematic of the optical transitions and atomic structure of $^{171}Yb^{+}$ relevant to state initialization. An applied magnetic field lifts the degeneracy of the Zeeman levels. Those levels necessary to for a typical initialization scheme are shown in the diagram. Dashed lines represent spontaneous decays, while solid lines indicate driven transitions.

2.4 Coherent Excitations

2.4.1 The Bloch Sphere and the Bloch Equations

Many useful experiments and operations in a quantum computer are carried out in the "coherent" regime, where the induced dynamics occur quickly compared to dissipation. The basic building block of an ion trap quantum computer is a qubit: a single two-level system. I will first talk about the free dynamics of a qubit, and then discuss its interaction with an applied radiation field. The two-level Hamiltonian is here written as

$$H_0 = \begin{pmatrix} E_0 & 0 \\ 0 & E_1 \end{pmatrix}, \tag{2.15}$$

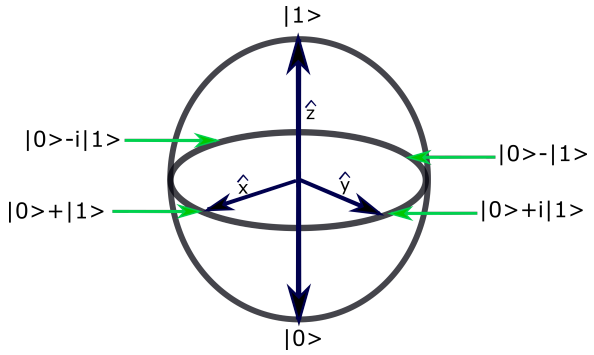

Figure 2.5: Diagram of the Bloch Sphere, a construct which allows us to represent an arbitrary superposition of a two-level system.

where E_0 and E_1 are the energies of the lower and upper eigenstates $|0\rangle$ and $|1\rangle$. An arbitrary wavefunction of the system can be written as

$$\Psi(t) = C_0 e^{i\frac{E_0}{\hbar}t}|0\rangle + C_1 e^{i\frac{E_1}{\hbar}t}|1\rangle \quad (2.16)$$

$$= \cos(\theta/2)|0\rangle + \sin(\theta/2)e^{i\phi}e^{i\omega t}|1\rangle\,. \quad (2.17)$$

Here C_0 and C_1 are arbitrary complex numbers, $\omega = (E_1 - E_0)/\hbar$, and θ and ϕ are spherical angles. I omit an overall phase which is irrelevant in the two level case. The second form of the above equation is useful when we use a mathematical representation of a two-state system called the Bloch sphere. On the Bloch sphere, a pure state is represented as a vector of unit magnitude. As shown in figure 2.5 the two eigenstates lie at the north and south poles, and superpositions with different phases lie along the equator. For the arbitrary state written above the polar angle is given by θ and the azimuthal angle is equal to ϕ, and the state rotates at the frequency ω around the z axis.

We now apply a near-resonant oscillating potential

$$V = \hbar\Omega[\cos((\omega+\delta)\mathrm{t})\sigma_\mathrm{x}], \quad (2.18)$$

where Ω is the Rabi frequency, δ is the detuning of the oscillating potential from the resonance, and σ_x is the Pauli matrix. Using the time dependent Schroedinger equation we

can straightforwardly find the time evolution of C_0 and C_1 to be

$$i\dot{C}_0 = C_1(e^{i\delta t} + e^{-i(\omega+2\delta t)})\frac{\Omega}{2} \tag{2.19}$$

$$i\dot{C}_1 = C_0(e^{i(\omega+2\delta t)t} + e^{-i\delta t})\frac{\Omega}{2}, \tag{2.20}$$

where $\Omega = \frac{\langle 0|\mathbf{U_0}|\mathbf{1}\rangle}{\hbar}$ is the Rabi frequency. We can recast these dynamics in terms of the Bloch sphere. To make the connection to the Bloch sphere it is useful to recast our variables in a different form. We consider the combinations

$$u = 2\Re(C_0 C_1^* e^{i\delta t}) \tag{2.21}$$

$$v = 2\Im(C_0 C_1^* e^{i\delta t}) \tag{2.22}$$

$$w = |C_0|^2 - |C_1|^2 \tag{2.23}$$

Where u, v, and w are the x, y, and z components of the Bloch sphere representation of $|\Psi\rangle$. Using 2.19 and 2.20, their time derivatives can be found to be

$$\dot{u} = \delta v \tag{2.24}$$

$$\dot{v} = -\delta u + \Omega w \tag{2.25}$$

$$\dot{w} = -\Omega v. \tag{2.26}$$

Together, these are the Bloch equations. They can be written in vector form as

$$\dot{\mathbf{R}} = \mathbf{R} \times \mathbf{W} = \mathbf{R} \times (\Omega\hat{x} + \delta\hat{z}), \tag{2.27}$$

with $\mathbf{R} = u\hat{x} + v\hat{y} + w\hat{z}$ being the Bloch vector, which precesses around $\mathbf{W} = (\Omega\hat{x} + \delta\hat{z})$, which is only dependent on excitation field parameters. By controlling the Rabi frequency, detuning, and time duration of the applied electric field, we may control the evolution of the state.

2.4.2 Rabi flopping and single qubit rotations

We would like to shuttle population from one of our states to the other, e.g. $|0\rangle$ to $|1\rangle$. Now that we have dervied 2.27 it is easy to see how to do so; we simply apply radiation with detuning δ and Rabi Frequency Ω near the atomic resonance for a specific duration. The

state initially in $|0\rangle$ rotates about the vector $\mathbf{W} = \Omega\hat{x} + \delta\hat{z}$. Simple geometric considerations on the Bloch Sphere will give the maximum overlap with state $|1\rangle$ to be Ω^2/W^2, and the rotation rate as $W/2$. The population oscillates between the two states, with excited state population

$$|b|^2 = \frac{\Omega^2}{W^2}\sin^2(Wt/2), \tag{2.28}$$

where $W^2 = \Omega^2 + \delta^2$ is the generalized rabi frequency. This phenomenon is called Rabi Flopping. By leaving the radiation on for a controlled duration, arbitrary rotations about $\mathbf{W}$ can be achieved. If $\delta = 0$, then we rotate about the $\hat{x}$ axis and achieve full population transfer. Furthermore, by allowing for phase evolution of the qubit we can effectively perform rotations about $\hat{z}$ axis. Given two orthogonal generators of rotation we may create any arbitrary rotation on the Bloch sphere, so we can arbitrarily manipulate a single qubit.

2.4.3 Single ion motional excitation

Because of the momentum kicks that absorption and emission cause, it is possible to drive transitions which not only change the atomic state of our ion but also change its motional state in the trap. These excitations turn out to be very useful. We consider the same two-level hamiltonian as before, but with the addition of a harmonic trapping potential which we treat fully quantum mechanically.

$$H = \hbar\omega_0 |0\rangle\langle 0| + \hbar\omega_1 |1\rangle\langle 1| + \hbar\omega_x(a^\dagger a), \tag{2.29}$$

where ω_x is the trap frequency and a and $a^\dagger$ are the motional creation and annihilation operators. We must now write the state vector including a summation over the harmonic oscillator states n:

$$|\Psi\rangle = \sum_{i=0}^{1}\sum_{n=0}^{\infty} C_{i,n}\,|i\rangle\,|n\rangle\,. \tag{2.30}$$

This system is joined by a potential oscillating at ω_{int} of the form

$$H_{int} = \hbar\Omega\left(|0\rangle\langle 1| + |1\rangle\langle 0|\right)\left(e^{ik_x x + i\omega_{int}t} + h.c.\right). \tag{2.31}$$

We now transform the Hamiltonian into the interaction picture and make the rotating wave approximation. We find

$$H = \hbar\Omega\left(|0\rangle\langle 1|\exp\left(i\eta(ae^{-i\omega_x t} + a^\dagger e^{i\omega_x t}) + i(\omega_{int} - \omega_0 + \omega_1)t\right) + h.c.\right), \tag{2.32}$$

where $\eta = \sqrt{\omega_{recoil}/\omega_x}$ is the Lamb Dicke parameter. This factor compares the recoil energy of a single photon of the radiation field to the quantized energy spacing of the motional harmonic oscillator. Smaller ratios indicate stronger suppression of motional transitions, because a single photon is no longer energetic enough to effect a change in the motional oscillator. Using the time dependent Schrodinger equation we now find:

$$\dot{C}_{1,n'} = -i^{(1+|n'-n|)} e^{(-i(\delta t-\phi))} \Omega_{n',n} C_{0,n} \tag{2.33}$$

$$\dot{C}_{0,n} = -i^{(1-|n'-n|)} e^{(i(\delta t-\phi))} \Omega_{n',n} C_{1,n'}, \tag{2.34}$$

where δ is the detuning from the $n' - n$ resonance, and

$$\Omega_{n,n'} = \Omega \left| \langle n' | \exp\left(i\eta(a + a^\dagger)\right) |n\rangle \right| \tag{2.35}$$

$$= \Omega e^{-\eta^2/2} \left(\frac{n_<!}{n_>!}\right)^{1/2} \eta^{|n-n'|} L_{n_<}^{|n-n'|}(\eta^2), \tag{2.36}$$

is a modified Rabi frequency, where L_n^α are the generalized Laguerre polynomials. Here we define the smaller of n and n' to be $n_<$ and the larger to be $n_>$. In the Lamb-Dicke limit $\eta^2(n+1) << 1$, the above form can be found to lowest order in η to be

$$\Omega_{n,n'} = \Omega_{n',n} = \Omega \eta^{|n'-n|} (n_>!/n_<!)^{1/2} (|n'-n|!)^{-1}. \tag{2.37}$$

Laplace transforms can be used to solve equations 2.33 and 2.34, but the full form is rather cumbersome. Additional resonances appear at $\pm(n' - n)$ for transitions to add or remove $(n'-n)$ motional quanta. Two simplified cases of the solution are used in this thesis; the first is weak excitation from $|0\rangle$. We excite near a resonance, so $\delta \ll \omega_x$. Under weak excitation $C_{0,n} << 1$ and $C_{1,n'} \approx 1$. Then the population transferred to $|1\rangle$ is

$$|C_{1,n'}|^2 = \Omega_{n',n}^2 \frac{\sin^2 \delta t/2}{\delta^2}, \tag{2.38}$$

In the other case the detuning δ from the nearby resonance is zero, and we can find:

$$\begin{bmatrix} C_{1,n'}(t) \\ C_{0,n}(t) \end{bmatrix} = \begin{pmatrix} \cos \Omega_{n',n} t & -ie^{i[\phi + \frac{\pi}{2}|n'-n|]} \sin \Omega_{n',n} t \\ -ie^{-i[\phi+\frac{\pi}{2}|n'-n|]} \sin \Omega_{n',n} t & \cos \Omega_{n',n} t \end{pmatrix} \begin{pmatrix} C_{1,n'}(0) \\ C_{0,n}(0) \end{pmatrix} \tag{2.39}$$

We can now see that the solution shows oscillations between the two levels at each resonance frequency $\omega_{int} = (\omega_0 - omega_1) + \omega_x(n' - n)$, corresponding to additional transitions.

These transitions correspond to the addition (removal) of $n \pm n'$ phonons from the motional mode of the ion, along with the previously discussed change in atomic state. The difference between this equation and pure Rabi flopping are changes to the Rabi frequency Ω (as mentioned before) and detuning δ

$$\Omega_{n,n'} = \Omega \left| \langle n' | \exp\left(i\eta(a + a^\dagger)\right) | n \rangle \right| \tag{2.40}$$

$$= \Omega e^{-\eta^2/2} \left(\frac{n_<!}{n_>!}\right)^{1/2} \eta^{|n-n'|} L_{n_<}^{|n-n'|}(\eta^2), \delta_{n,n'} \quad = \omega_{int} - \omega_1 + \omega_0 - \omega_x(n' - n), \tag{2.41}$$

Note that the sensitivity of the Rabi frequency to the motional numbers n and n' allows us to measure them, which we will do later. Toward that purpose, consider the following case. The ion is initially in an arbitrary motional state but a defined atomic state $|0\rangle |n\rangle$. A laser is now tuned to the resonance corresponding to $n' - n$. The population in the state $|1\rangle |n'\rangle$ becomes

$$|b|^2 = \frac{\Omega_{n',n}}{W_{n',n}} \sin^2(W_{n',n} t/2), \tag{2.42}$$

where $W_{n',n} = \Omega_{n',n} + \delta_{n',n}$ is the modified generalized Rabi frequency.

This picture needs a few flight modifications for usage in our trap. In three dimensions a $\cos\theta$ geometric factor multiplies the Lamb-Dicke parameter, resulting from the overlap of the wavevector with the particular trap axis being addressed (θ is the angle between the two). If there is little overlap, absorption or emission of photons from or into the laser beam will not give the ion recoil momentum on that axis. Furher generalizing the result to multi-ion chains requires first calculating the eigendecomposition of the normal modes of said chain. The effect of altering the vibrational motion to accomodate the normal mode picture is that the Lamb-Dicke parameter is modified by the magnitude of the eigenvector component for the particular mode and ion being excited[30]. $\eta \to \eta\beta_{i,j}$ where $\beta_{i,j}$ is the eigenvector component for the ith ion in the jth mode. The ions also have different Rabi frequencies due to their different positions in the tightly focused beam, so $\Omega \to \Omega_i$.

2.5 Normal Modes

We numerically solve for the normal modes of motion in the following way. We first consider only the axial direction and initiate the ions with even spacing roughly commensurate with

their typical spacing in the trap. Considering only the axial direction, we sum the coulomb and trap potentials

$$V_{total,axial} = V_{coulomb,axial} + V_{trap,axial} = \sum_{i=1}^{n} m_i \omega_x^2 x_i^2 + \sum_{j,m=1}^{n} \frac{kq^2}{|x_j^2 - x_m^2|}, \tag{2.43}$$

where the x_i are the ion positions, ω_x is the trap strength in the axial direction, k is the electric force constant, and q is the charge. We minimize this potential to find the equilibrium ion positions. We could simply use precalculated ion positions from **??**, but this method has the advantage that it will work for quartic potentials, which we explore in section **??**. We might also worry about transitioning away from a linear chain if we had too many ions in our chain, but we can observe and avoid the "zig-zag" transition in our calculation because it is made apparent by the softening of the lowest transverse vibrational mode to zero frequency. Once we find the equilibrium positions we expand the full trap potential

$$V_{total} = \sum_{i=1}^{3n} m_i \omega_i^2 x_i^2 + \sum_{i,j=1}^{3n} \frac{kq^2}{|\mathbf{x_i^2} - \mathbf{x_j^2}|} \tag{2.44}$$

around the equilibrium ion positions to find the normal mode vibrational frequencies.

In a chain with only one species of ions, certain features of the vibrational spectrum are simple. The highest frequency transverse mode oscillates at the same frequency as a single ion, and the lowest frequency axial mode does the same. The axial modes are also spaced evenly[31]. The spectrum changes considerably when ions of a different species are introduced. Even at a mere 25% mass difference, operation at typical trap parameters will cause the transverse modes to completely decouple. Taking a four ion chain as an example in figure 2.6, we can see that there are two vibrational modes clustered near the single barium ion radial frequency, and two vibrational modes near the single ytterbium ion radial frequency. Further, we can see that the eigenvector components for the ion oscillating in the mode at the radial frequency of the other species is tiny. In this figure the small eigenvectors are on the order of .01. The eigenvectors being so small presents significant problems for using these modes as a quantum information bus, as the coupling between spin and motion is very weak.

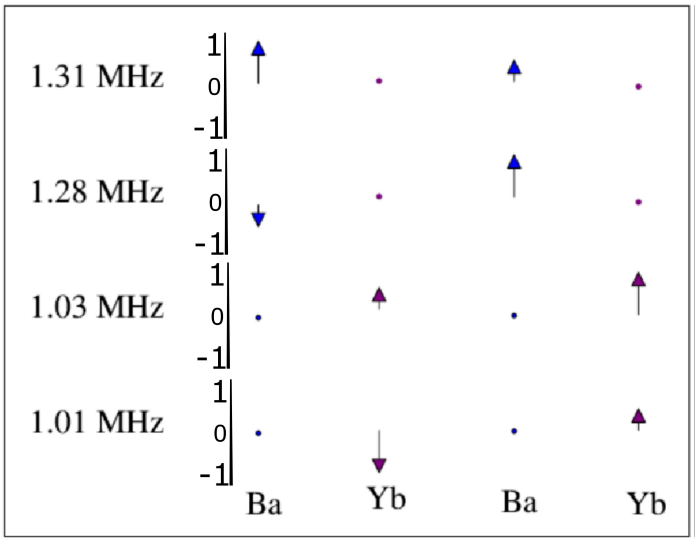

Figure 2.6: Normal modes of a chain of Ba-Yb-Ba-Yb ions. The vibrational frequencies are listed on the left and a scale is set next to each mode. The size of each arrow indicates the magnitude of that eigenvector component. The large arrows are ∼0.4-0.9 and the small arrows(dots) are ∼.03. The ion identities are along the bottom.

Chapter 3

EXPERIMENTAL APPARATUS

3.1 General Description of Apparatus

3.1.1 Barium

The details of our Ba^+loading scheme have been covered well by previous group members' theses[32] and experimental papers[33], so I do not discuss them here in detail. It suffices to say that we load from an atomic oven and achieve isotope selectivity through our photoionization scheme. To perform Doppler cooling we use two diode laser systems. One of the laser systems is a Toptica ECDL at 986 nm that we frequency double via SHG with a fiber pigtailed PPLN crystal to 493 nm. Barium's $6P_{1/2}$ state also decays to a long-lived (80s) $5D_{3/2}$ state with branching ratio 0.25, so to cool the ion continuously we apply a repump laser at 650 nm, generated by another Toptica ECDL resonant with the $5D_{3/2}$ to $6P_{1/2}$ transition. The ion is rapidly evacuated from the $5D_{3/2}$ state given the high laser power and broad natural linewidth. The strong coupling between $6P_{1/2}$ and $5D_{3/2}$ creates a new technical difficulty due to interference effects between the 650 nm and 493 nm lasers. Because of interference between the two electronic pathways, the correct frequency setting for the Doppler laser becomes a sensitive function of the repump laser power and frequency.

Both ECDL's have short term stabilities of 1-3 MHz but can exhibit drifts of $\sim$1MHz/min depending on laboratory conditions. Experimental runs range from 15 minutes to many hours and can easily be disrupted by ions delocalizing (if the lasers drift blue) or by insufficient fluorescence from the ions (if they drift red). Also, I perform experiments later to measure sympathetic cooling of ytterbium by barium, and so control of the temperature directly influences one of my measurements. For these reasons the Doppler cooling laser frequencies are locked to external reference cavities. The laser locking systems do not attempt to narrow the laser spectra but rather hold the center frequencies constant, so the reference cavities have moderate linewidths of about 100 MHz. The modest cavity finesse eases

alignment requirements for optical coupling. The reference cavities consist of two dielectric mirrors spaced ∼8 cm apart by invar and temperature stabilized with heaters controlled by a microcontroller. The cavities are held under weak vacuum of ∼1 torr, which should insulate them from ambient pressure and temperature swings. The reference cavities are all in the same vacuum container, and temperature crosstalk due to radiation may contribute to their instability.

The lasers are stabilized to the reference cavities with a top-of-the-fringe lock. A portion of each of the laser output is sampled and then frequency shifted and modulated by an AOM. After the AOM, the beams are sent to the reference cavities, and the signal is detected on the backside of the cavity by a photodiode. A lock-in amplifier demodulates the photodiode signal to create an error signal, and a PID circuit uses it to maintain the laser frequency. The setup for the 986 nm laser is shown in 3.1, and the 650 nm setup is very similar. Previously the AOMs for both cavity locks were in the double-pass configuration. This allowed for an adjustable offset between the laser frequencies and the cavity lines; however, the optical setup was non optimal and significantly reduced the mode quality and transmitted power. A top-of-the-fringe lock is in principle insensitive to the overall transmitted laser power, but in practice the noise floor of the detectors and lock-in cicrcuitry is fairly high, and the amount of power transmitted strongly affects the ability of the locking system to remain on specific cavity lines. The coupling of the laser to the reference cavity also significantly affects the stability of the locks, and the previous poor spatial mode worsened the lock performance, making it more likely to jump cavity lines. Changes to the pointing of the laser upstream of the cavity have a strong effect on the phase of the transmitted signal, and without proper adjustment the lock does not hold on well.

Currently, I have reconfigured the reference cavity modulation AOMs into single pass configuration. The extra power and the cleaner laser mode give clear benefits in terms of the locks' stability. Unfortunately, the tuning of the lock system must be done via temperature control of the reference cavities, although in principle it would be better to leave the temperature control untouched to achieve the greatest long-term stability. After the present experimental run is finished we plan to change the configuration back to a double pass, but to retain good optical quality we will use longer focal length lenses.

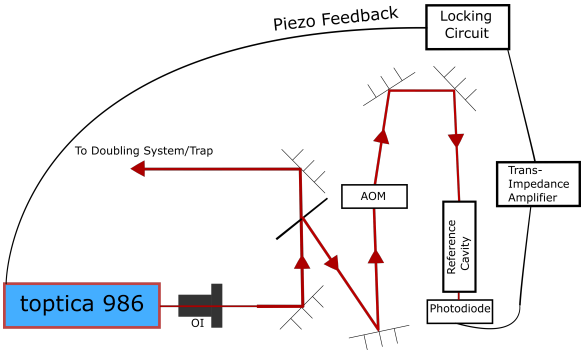

Figure 3.1: Mixed optical and electronic diagram of the 986 nm laser locking scheme. Part of the laser output is broken off and frequency modulated by an AOM. The beam is then passed through a reference cavity and illuminates a photo diode, whose signal is sent through a transimpedance amplifier. The locking system demoulates the signal and feeds back onto the laser to keep it on resonance.

3.1.2 Ytterbium

Yb^+ has a simple atomic structure which requires only one repump laser, and a cycling transition that can be used for state detection and Doppler cooling(see fig 3.1.2). Though not as long wavelength as barium, ytterbium's 369 nm Doppler cooling transition is accessible with commercially available diode lasers, unlike many other ions used for quantum information. At present, our Doppler cooling lasers are not tuned to Yb^+'s atomic resonance, so we sympathetically cool ytterbium using barium. The appearance of ytterbium in the ion chain is identified by visible shifts in the ion positions, and verified with vibrational mode spectroscopy combined with numerical simulations.

We have fabricated a 369 nm diode laser in a Littrow configuration for Doppler cooling ytterbium. Currently, we can only tune the central frequency and feedback of the Doppler cooling laser at room temperature, but the laser must be cooled down to $-15°$ Celsius to operate at 369 nm. Cooling the laser from room temperature requires tens of minutes so tuning is slow, and if the grating arm drifts mechanically the upkeep is burdensome, though we could potentially install a picomotor to reposition the grating arm while the system is

Figure 3.2: Yb^+ atomic structure and the lasers required for Doppler cooling. The 369 nm transition is strong, and because the branching ratio to $5D_{5/2}$ is only 0.005, the ion repeatedly "cycles" on the 369 nm transition. This property makes Doppler cooling and state detection of $^{171}Yb^+$ simple. When the ion does decay into $5D_{5/2}$, a 935 nm laser excites the ion into a nuclear shell excited state from which it decays back into the ground state.

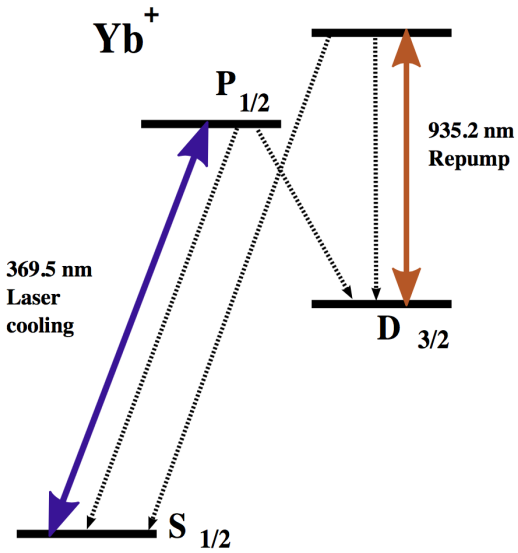

cold.

We also fabricated a complete 935 nm repump laser system to remove population from ytterbium's long-lived $5D_{3/2}$ metastable state. This repump system allows for continuous Doppler cooling. We built a reference optical cavity of the same design as the barium reference cavities, and have measured that the laser frequency is stabilized to within 10 MHz. The excited state in the 935 nm transition does not decay to any other state, so the cooling cycle is closed. There is an additional problem due to Ytterbium's level structure-occasionally (a few times per hour) it can be excited to a long-lived dark metastable state $F_{7/2}$, which can be repumped with 638 nm light. A bare laser diode at 638 nm directed into the trap should be adequate to repump these levels.

We are currently working with $^{176}Yb^{+}$ because our ionization source is locked to that line (it is borrowed from Professor Subhadeep Gupta's lab). Eventually though, we would like to work with $^{171}Yb^{+}$, which has a 12.6 GHz hyperfine splitting in the ground state. The standard technique for bridging the hyperfine structure uses optical modulators to bridge the large hyperfine splittings in ytterbium. Instead, I propose the following: assume that our ion starts off in in ground state in either the F=0 or the F=1 manifold. In order to cool, initially we apply 369 nm light resonant with the $6S_{1/2}$ F= 1 to $6P_{1/2}$ F= 0 transition, along with microwaves at 12.6 GHz to evacuate the F= 0 manifold of the ground state. The ion will be optically pumped to the $5D_{3/2}$ F= 1 manifold. At this point we turn off the 12.6 GHz excitation and turn on the 935 nm laser, resonant with the F= 1 to F= 0 transition. The cooling cycle is now closed, and the ions should only go dark due to occasional off-resonant excitation, but they can always be reset by applying the same procedure. We can perform state detection by following the above protocol without the use of the 12.6 GHz excitation. In order to optically pump we still require an AOM, but we can make the modulation requirements easier to fulfill by modulating the 935 nm light instead of the 369 nm light. We then need to bridge a gap of only 1.4GHz (instead of 2.2) in the infrared (which is easier than in the UV). To optically pump, we apply RF at 0.83 GHz and add a 1.4 GHz sideband to our 935 nm laser to drive the $5D_{3/2}$ F= 2 to the $5D[3/2]_{1/2}$ F= 0 level. $5D[3/2]_{1/2}$ decays part of the time to the $6S_{1/2}$ F= 0 ground state, and all other levels are coupled to $5D[3/2]_{1/2}$, so we optically pump to $6S_{1/2}$ F= 0.

3.2 Imaging the Ions

Reductions in available personnel demanded that I fix certain technical problems which had previously been manageable. The oven in our experimental chamber was not producing barium consistently. At times it was taking over an hour to trap and there were week long periods during which I could not trap at all. This made experimental progress very slow, so I decided to break vacuum and insert a new oven. In replacing the oven, I swapped the top viewport from the cumbersome bellows system we had tried to use previously to a simple flat viewport. In doing so, I did not consider that the bellows viewport was "re-entrant", or in other words that the old viewport had a depression which allowed for closer optical access to the trap. As a result, no available commercial microscope objective had a long enough working distance for use with my ion trap.

I did not want to sacrifice signal as doing so would greatly increase my experimental run times, and I did have a very large top viewport to play with, so I decided to try using a 2 inch diameter plano-convex lens as my primary imaging stage. Unfortunately, without any compensation lenses the high numerical aperture resulted in severe optical abberations. Detection with the PMT was about half as fast as before, so I was still collecting a reasonable amount of light using the large primary, but the fluorescence was spread out over a very large area. Images of ions taken with our camera showed that the ion images had a bright central feature corresponding to a normal ion image, but then had large weak haloes which compromised most of the collected light.

I believed that spherical abberation might be the problem, so we made optical simulations of the imaging setup using OSLO. We measured all distances in the optical setup to $\sim$1 cm accuracy, and kept the same basic configuration(a confocal microscope), with both the primary and secondary producing about a factor of 7 in magnification. We simulated an ashperical lens with an NA of 0.1 (available from Thorlabs) as our primary, and the results suggested that we could obtain good image quality(see figure 3.2). We purchased said lens and mounted it on the imaging stage. The images are shown in fig. 3.4- in these simulations I had not taken into account that the moderately large numerical aperture of the system would make it sensitive to optical abberations. Some reduction in abberation was achieved

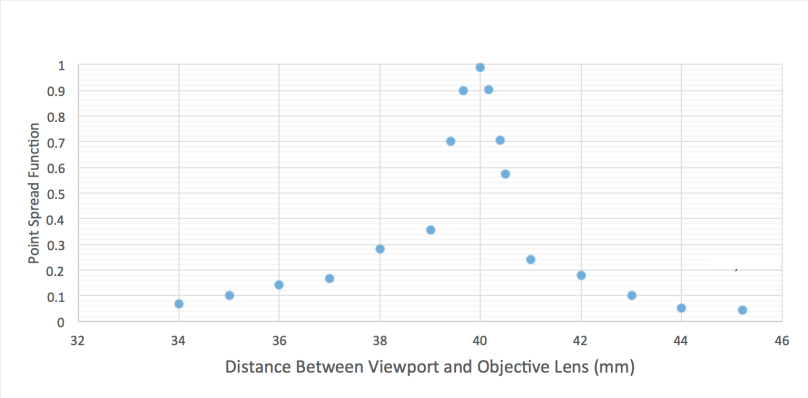

Figure 3.3: Numerical calculations of the maximum of the point spread function and relative intensity for imaging 493 nm light using the aspherical lens. There is a clear optimum at about 40 mm, and a FWHM of about 1 mm. The positioning of the imaging system has a very narrow working range.

by forcing the primary and secondary lenses onto the same axis using a lens tube, but despite sustained efforts over the course of several weeks I was unable to achieve reasonable image quality. Perhaps worse, the system was strongly chromatic, so it is impossible to simultaneously image the fluorescence of $Ba^{+}$and Yb^{+} . The simulations were repeated independently by a master's student with the same result, so I believe they were actually accurate. We simply aren't able to achieve the alignment or working distance necessary to make the system work.

I could obtain only modest improvements in image quality from optical adjustments, so I decided to try post-processing with a technique common in biophysics and astronomy, image deconvolution. I acquired a long exposure image of a single ion and found the distribution of light it gave off. We are in a fairly unique position in ion trapping in that we can acquire the exact image that a point source creates in our imaging system. Ideally I could use either cross-correlation (Wiener) or a maximum likelihood method (Richardson-Lucy) to find the brightnesses given a short exposure image of multiple ions. Raw images from our microscope are shown in figure 3.2 and the deconvolution results are shown in figures 3.2 and 3.2. Wiener deconvolution is the most straightforward implementation of deconvolution,

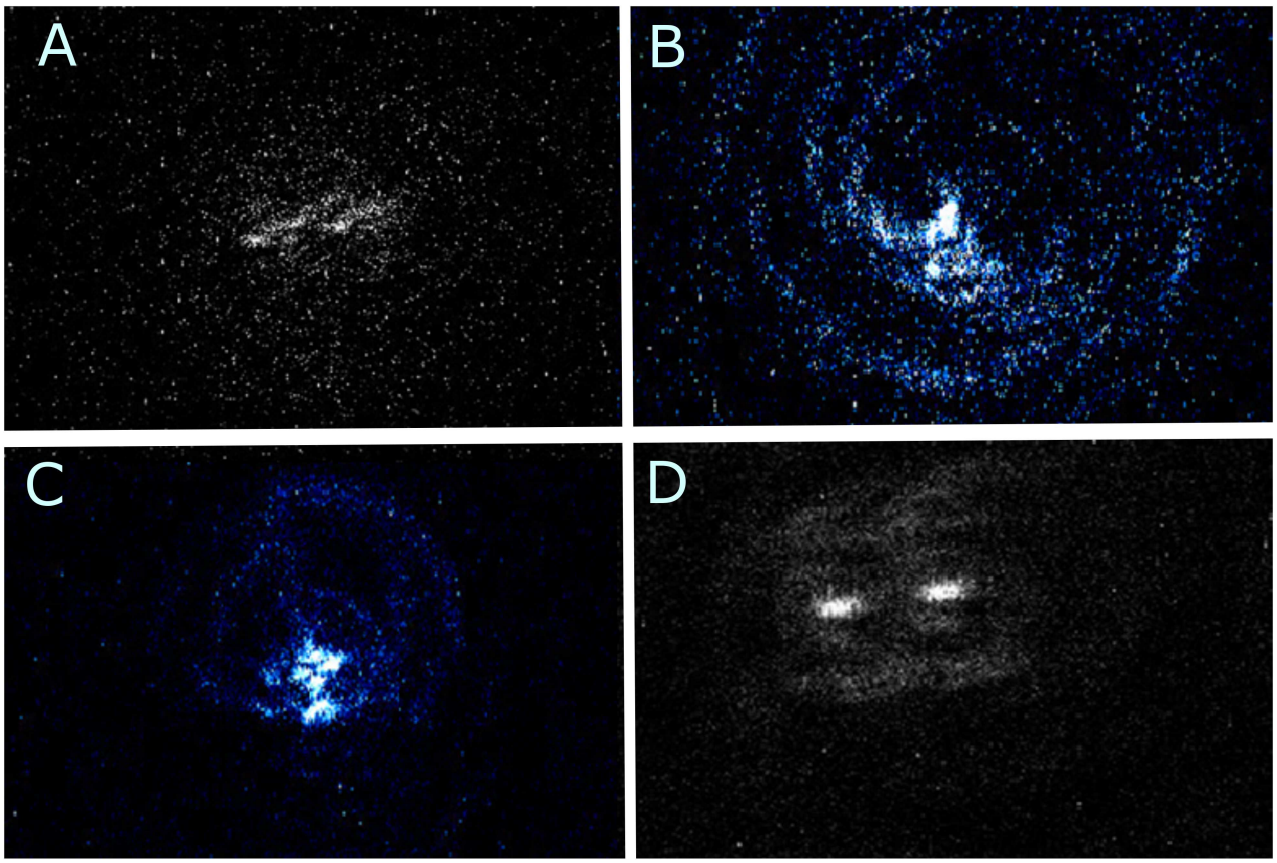

Figure 3.4: Ion images taken after the trap was rebuilt. a) Image of two ions taken using a plano-convex lens. b) The image (here of one ion) changed after insertion of an aspherical lens, but we were initially far away from the correct working distance, and still had significant aberation due to coma. c) Image of one ion after attempted adjustment to the optimal working distance for the aspherical lens. d) Image of two ions after constricting the system to have fairly low coma. The image quality did improve significantly but the majority of the collected fluorescence was still being thrown into a wide area around the ions.

Figure 3.5: Raw short exposure images of five Ba^+ions with our new microscopy setup. The ions are barely visible. There is significant overlap of the different ion images, and the ions towards the edge of the image are slightly dimmer.

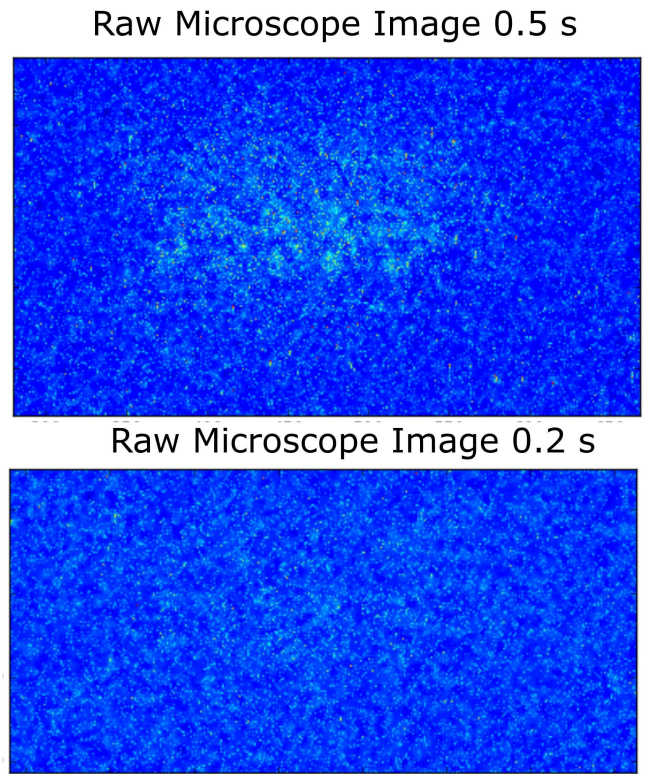

Figure 3.6: Wiener deconvolution applied to the same 5 ion images as in figure 3.2. The ions may appear to be clearer but analysis shows that the signal to noise ratio has not improved.

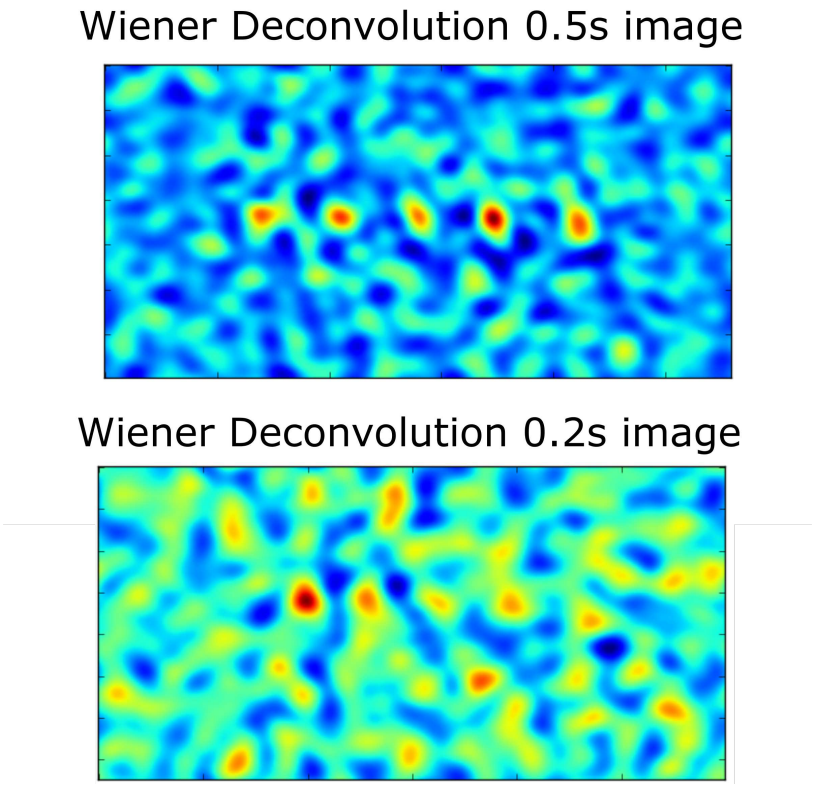

using cross correlation and a weighted filtering term which combats high-frequency noise[34]. The Wiener deconvolution either tended to overfit to noise, or to blur out the images of the ions depending on the weight given to the filtering term. The ion images are unnatural from an image processing perspective, because they give essentially delta-function impulses to the imaging system, which is why standard Wiener deconvolution tends to work very poorly.

Richardson-Lucy deconvolution is a maximal likelihood regression algorithm, and it produced good images when the signal from the ions was large enough, but it would regularly miss ions regardless of hyperparameter settings. I believe that the point spread function I had been working with was likely at fault. In images taken with 1 s exposure, the ion

Figure 3.7: Richardson-Lucy deconvolution of the same raw image as in figure 3.2. The ion positions are at the five well resolved dots in a horizontal row. This filtering technique produces well resolved ion images, but it can miss some ions entirely. Richardson-Lucy is an iterative Maximum Likelihood algorithm. The number of maximum likelihood iterations was varied to find the best deconvolution. Only the 0.5 s exposure is shown here, as the 0.2 s exposure was completely blank after attempted deconvolution.

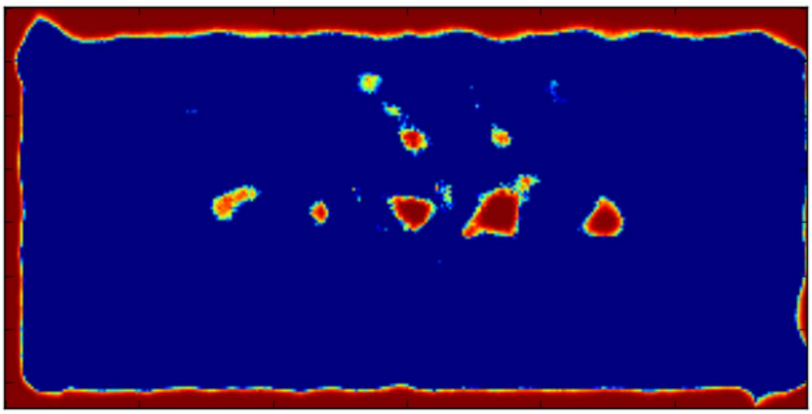

image moved by several pixels between frames. The images I took to create the point spread function used twenty minute long exposures to achieve good SNR, and so they were averaged over the meandering of our ion images, which made them effectively blurry. The instability in their apparent positions is due to the height and unbraced construction of the tower holding the camera. A better point spread function could be obtained by taking many short exposures with a single ion, and then matching the positions of the individual exposures using maximum likelihood methods. Alternatively, a significant improvement in image quality could be achieved using a short focal length camera lens as our objective; camera lenses are compensated for optical aberrations. It should also be possible to purchase one with a reasonable numerical aperture at this distance. The use of photographic camera lenses is mentioned in historic ion trapping papers[35]).

3.3 Raman gate laser system

Upon entry into the lab I embarked on building the laser system that could support two photon transitions which can be used for individual and ion-ion motional gates. The laser itself is a modified SpectraPhysics Vanadate CW pump laser into which I inserted a semiconductor saturable absorber mirror, or SESAM[36]. The semiconducting mirror causes the cavity to spontaneously mode-lock, so long as parameters related to the gain medium saturation and absorber mirror saturation are satisfied[37]. Additionally, the beam must be large enough at the gain medium to absorb a reasonable amount of power from the pump lasers, and the SESAM damage threshold must not be exceeded. Using gaussian beam optics I optimized the cavity parameters until all of the above conditions were satisfied and the laser also produced a collimated TEM00 output, see figure 3.8. After some minor modifications to the $50000 laser involving a bandsaw and a lot of epoxy, the laser produced pulsed output at 1064 nm, with a measured autocorrelated pulse width of 12 ps, limited by SESAM recombination parameter. The emitted light is then frequency doubled in a single pass through a non-critically-phase-matched LBO crystal, creating approximately 300 mW of 532 nm light.

The two photon transitions which we would like to drive require us to modulate our 532 nm laser to produce a beat note which is near-resonant with the ground state splitting of the ion[38]. We accomplish this by modulating the beam at two different frequencies, and then using the beat note to drive a transition between the ground state levels of Ba^+. The 300 mw output of the doubling stage is sent into a beam splitter and then shifted by using two AOM's. One beamline has an adjustable delay stage, which allows us to ensure that our two pulses arrive at the ion at the same time. The beams are then combined with a second PBS and then directed into the trap.

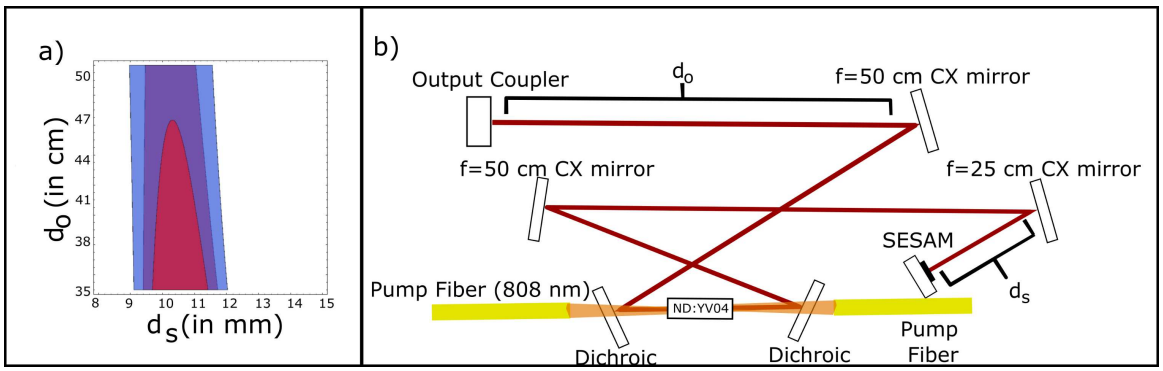

Figure 3.8: a) Diagram showing the overlap of various constraints for the mode locked laser. d_o and d_s are the output coupler and SESAM positions, respectively. They influence the size of the laser mode at the gain medium, on the SESAM, and at the output. Blue here indicates sufficient saturation of the SESAM, red is saturation of the gain, and purple is both. b) Schematic of the laser cavity. The Nd:YvO_4 Vanadate gain medium is pumped optically by two 808 nm fiber coupled laser bar diodes which generate 20W of light. d_o and d_s from part (a) are labelled on the diagram.

Chapter 4

A SINGLE TRAPPED ION

4.1 1762 single ion measurements

Before I proceed to discuss work with multi-ion mixed species chains, it makes sense to spend some time talking about similar experiments involving a single ion. We do so both to test methods we will later use with multi-ion chains, and to understand some systematics that crop up due to technical issues with our equipment. The central piece of equipment used in these measurements is a 1762 nm fiber laser and its associated locking system, initially configured by Mattew Dietrich[39]. The upshot of his prior work is that we have a laser source available for driving the narrow (mHz broad) $6S_{1/2}$ to $5D_{5/2}$ transition, which has varying stability at different timescales, but no worse than $\sim$10 kHz over the course of a few hours.

4.1.1 Shelving and 1762 characterization

A typical experiment using the 1762 nm laser proceeds as follows. A Ba^+ in the trap is first Doppler cooled, and then initialized to one of the two ground state levels via optical pumping. A 1762 nm pulse sequence is run, and the ion is prepard in a superposition state between $5D_{5/2}$ and the ground state. The Doppler cooling and $5D_{3/2}$ repump lasers are turned back on, illuminating the ion and collapsing it to either the ground state or a $5D_{5/2}$ state. If the ion collapses to $5D_{5/2}$ then the Doppler cooling light is not resonant with an available transition, and so the ion does not fluoresce. If the ion collapses to the ground state, it will cycle on the 493 nm and 650 nm transitions and emit fluorescence. In the window after the lasers are turned back on, the PMT counts are recorded and thresholded to determine if the ion collapsed to a bright ($6S_{1/2}$) or dark ($5D_{5/2}$) state. The experiment is repeated many times with the same parameters and the probability of excitation to $5D_{5/2}$ as a function of the particular 1762 nm settings is recorded.

Previous attempts at characterizing the 1762 nm laser frequency stability yielded seemingly inconsistent results. Fits from adiabatic rapid passage sweeps gave a linewidth of 100 Hz[40], whereas frequency scans across carrier transitions showed a minimum non-power-broadened linewidth of ∼5 kHz[39]. The critical point which allows for reconcilliation of these two measurements is the difference in timescales. Adiabatic rapid passage experiments depends weakly on the starting and ending frequencies of the sweep, but so it is only sensitive to the laser's stability during a single sweep. The laser only needs to be stable for the duration of a single pulse, 200 ms or less, which results in sensitivity to noise only above 50 Hz. Sideband scans take several minutes to cross the line and are therefore sensitive to noise in the sub millihertz range. I repeated Matt Dietrich's measurements of power broadening of a $6S_{1/2}$ to $5D_{5/2}$ carrier transition and measured the same 5 kHz HWHM of a carrier transition, shown in figure 4.1.

By speeding up our sideband scans, I attempted to investigate whether I could determine the spectral range where the noise exists. Previously, these scans were done slowly in order to build up good statistics. Instead, I took data with each individual run having only about 20 runs per data point. Each datapoint now has a large statistical error, but the fitted widths remain consistent with the higher-run data, and the error on the width does not grow dramatically. For our 50 ms experiment time each data point should take about a second, and with a feature width of five data points this means we should not be sensitive to any noise slower than ∼0.2 Hz. The results are shown in fig 4.2. The HWHM of the transition is reduced from ∼6 kHz to ∼3 kHz, so our noise is in the sub-Hz region.

4.1.2 Drift & Repeatability

Our group had previously seen slow long term drifts of the 1762 nm laser but had never measured it nor characterized any variations in it. As part of the experiments I'll speak about in Chapter 5 I measured the same carrier frequency for two months. The drift over different timescales is shown in figures 4.3 and 4.4. The stability over the course of a day is not totally consistent with a linear drift, but the linear drift is a significant part of the behavior. Over the long term the drift appears to be stable. It is large enough to cause

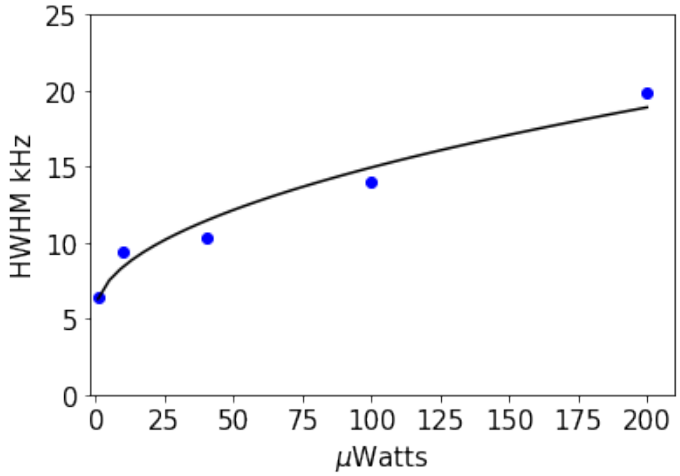

Figure 4.1: Broadening of a 1762 carrier transition as a function of power. Each data point is the fitted width of a peak from a sideband scan. The fitted minimum half width is ∼5 kHz.

curve fitting problems during our longer frequency scans, as the data point positions are shifted slightly from their true values.

During sideband scans of multi-ion chains a stronger effect comes into play. Our RF trap frequencies drift during these long scans due to changes in our RF power coupling. The drift is shown in figure 4.5. Because of the drift it becomes impossible to obtain good fits for our sideband scans, so we must add several offsets to the frequencies of our peaks as free parameters. In our less dense frequency scans this poses no problem as the peaks are well resolved, but in scans where the peaks are close together, it becomes possible to misidentify the location of one or more peaks. We could possibly improve the stability of our RF power by using stiffer and better made cabling between the source, amplifier, and RF resonator. We could also passively stabilize the temperatures of both our can and amplifier, or actively stabilize the RF power entering the trap. Using these techniques ppm stabilities have been achieved[21].

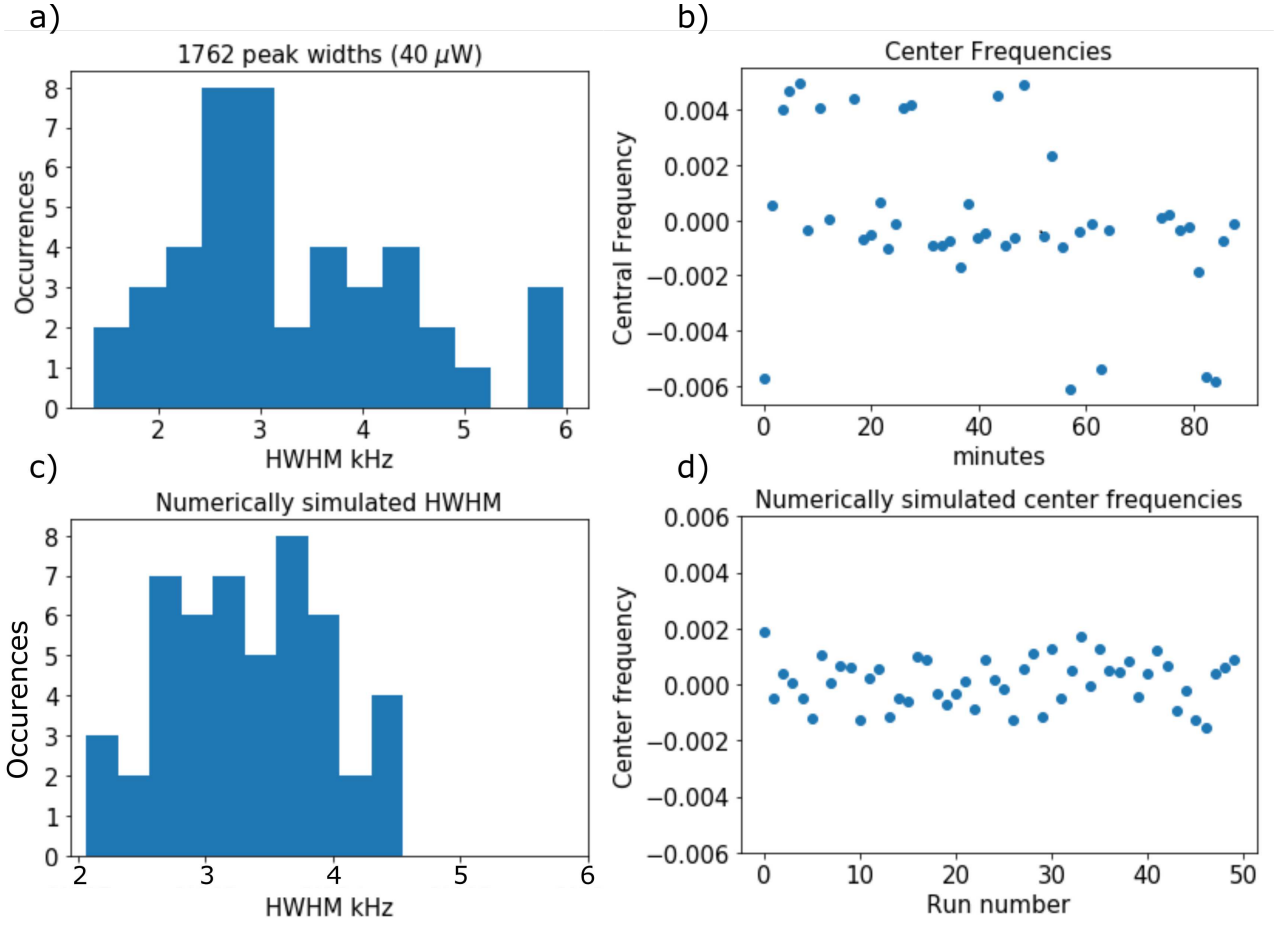

Figure 4.2: Fitted widths and center frequencies of fast frequency scans taken with 20 runs per point, and numerical simulations of the same. **a**) A histogram of the fitted peak widths from our 20 run scans. The mean HWHM here is 3 kHz. **b**) The distribution of carrier frequencies showed an odd trimodal behavior. I was worried that perhaps our sampling of the widths was being affected by the low numbers of runs in our experiment, so I did numerical simulations of the data taking. **c**) A histogram of the numerically simulated widths, in qualitative agreement with the widths fitted from real data. **d**) The fitted numerically simulated center frequencies. These data do not display the trimodal behavior seen in b), but the spread around the center frequency is close to the spread seen around each center. The likely cause for the shifts here is the voltage resolution of the DAC of the microcontroller running the 1762 nm lock.

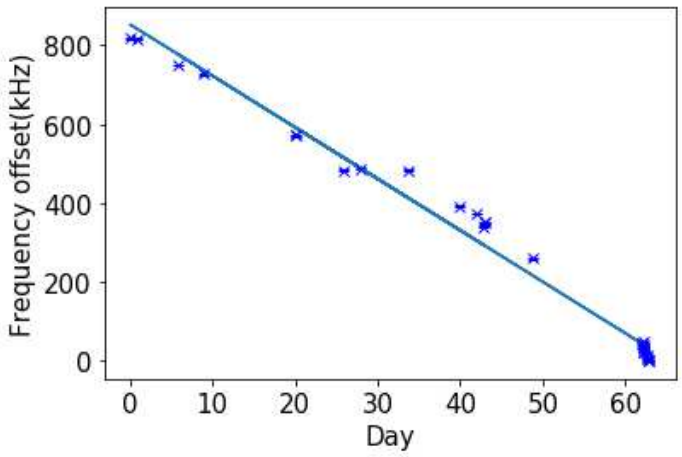

Figure 4.3: 1762 drift over several months: average of -13.05 kHz/day. Error bars are statistical, but too small to see.

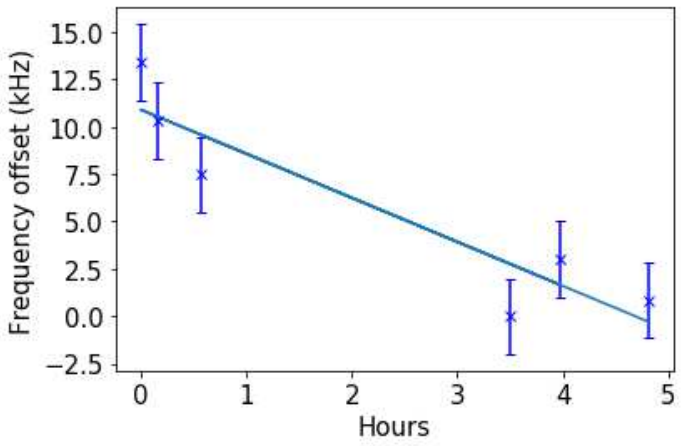

Figure 4.4: 1762 drift over a few hours, with an average of -2.34 kHz/hr. This is twice as fast as the drift seen over several months, showing some of the day-to-day variation in the drift of the lock. Error bars are statistical.

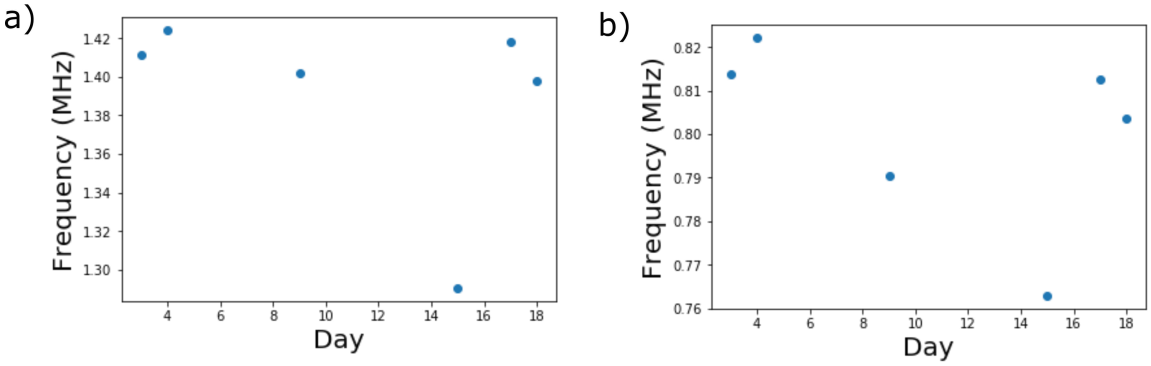

Figure 4.5: The drift of the upper (a) and lower (b) radial secular frequency sidebands of a single trapped Ba^+. The correlation between the plots indicates that a drift of our RF power is the cause, not a drift of the needle or squeeze voltages.

4.1.3 Temperature measurements of a single trapped Ba^+

Sympathetic cooling is one of the techniques that I mentioned early on in regards to mixed species ion chains that would prove very useful for a quantum computer. I would like to measure the temperature of a sympathetically cooled ion chain, but I should first check that my measurement is in good agreement with the Doppler limit for a single ion. Discussing the single ion measurement also serves as an introduction to the measurement technique. After initial trapping and Doppler cooling, our single ion is in a thermal motional state and its energy is distributed among x, y, and z trap axes. Each trap axis is a harmonic oscillator and they have motional quantum numbers n_x, n_y and n_z. After Doppler cooling the ion's motional state in each oscillator is a mixture distributed per the Maxwell-Boltzmann distribution. With some straightforward manipulations we can recast the distribution as (dropping the subscript on n):

$$P(\bar{n}, n) = \sum_{n=0}^{\infty} \frac{1}{\bar{n}+1} \left(\frac{\bar{n}}{\bar{n}+1} \right)^n, \tag{4.1}$$

where n is the energy level occupation number, $\bar{n}$ is the mean occupation number of the motional states, and $P(\bar{n}, n)$ is the probability of a given state n for a given $\bar{n}$. This distribution is shown for different values of $\bar{n}$ in 4.6. We can use $\bar{n}$ to characterize our

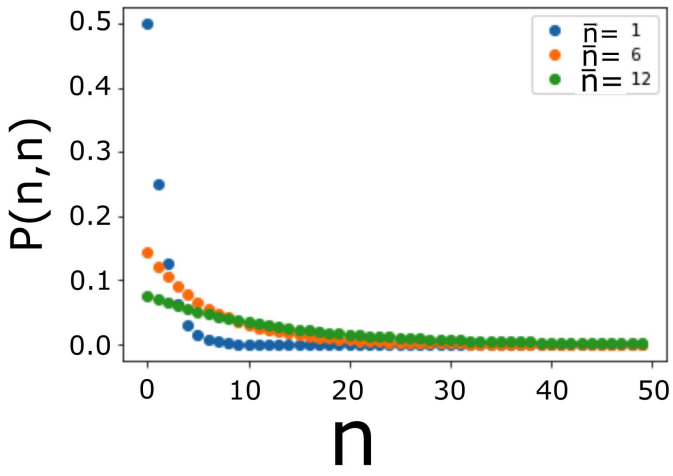

Figure 4.6: The occupation probabilities for different values of $\bar{n}$. Even moderately nonzero values of $\bar{n}$ lead to a wide spread of occupation numbers. For our 493 nm Doppler cooling transition an $\bar{n}$ of 7.5 corresponds to the Doppler limit.

trapped ion temperatures. I will now measure the efficiency of Doppler cooling for a single barium ion. Doppler cooling should result in the same temperature for all axes for a single ion, so I choose to excite the first blue secular motion sideband of the $6S_{1/2}$ to $5D_{5/2}$ transition in the radial $\hat{x}$ direction.

Here I diagnose the efficiency of Doppler cooling by measuring $\bar{n}$ for only one vibrational mode in the transverse direction. I do so by weakly exciting the first blue secular sideband corresponding to n_x.

Because the ion is in a thermal state the result of my experiment is a thermal average over the underlying coherent states. We should therefore combine equation 4.1 and equation 2.42, with $n' = n + 1$. Also note that our laser beam is coming in at 45° to the trap axis, so the Lamb-Dicke parameter η is reduced by $1/\sqrt{2}$. We obtain (on resonance):

$$\Omega_{n',n} = \eta\sqrt{n} \tag{4.2}$$

$$\Phi = \sum_{n=0}^{\infty} \frac{1}{\bar{n}+1}\left(\frac{\bar{n}}{\bar{n}+1}\right)^{n} \sin^2(\eta\sqrt{n}t/2), \tag{4.3}$$

Additionally, if the excitation is weak we can use the approximation shown in equation 2.38, and I stop to compare it to the full solution. The result of a weak excitation measurement on a radial sideband is shown in figure 4.7, along with fits to both equations. Both fit reasonably well, but there is a discrepancy in the meaured $\bar{n}$ of $\sim$20%. This will contribute significantly to error on our measurement here and later, but our qualitative results will remain the same. Note here that the measured temperature of our ion at $\bar{n} = 300$ was $\sim$30 times the Doppler limit. We attempted to verify this measurement by measuring the decay of a Rabi flop(fig 4.8), but we are limited by slow noise in our laser lock from definitively extracting a temperature from that measurement. Several different sources could have been the cause of the elevated measured temperatures. Stray fields which appear during loading could cause intense micromotion which would broaden the cooling transition and spoil the final temperature[41]. To check if that were the case, I locked my lasers to Doppler cool the atoms and continuously performed the same weak excitation measurement over the course of many hours, but I saw no significant reduction in temperature as would be expected if the stray fields were decaying.

4.2 Doppler cooling linewidth measurement

I was also worried that our Doppler cooling lasers could be at fault. To verify that no problem existed with our Doppler cooling setup, I measured the linewidth of our 493 nm transition. I note from equation 2.14 the dependence of the Doppler cooled temperature on the slope of the transition: a narrow linewidth results in a low temperature. Further, if micromotion is sufficiently large, heating occurs for for laser frequencies near the transition[41]. Figure 4.9 shows that so long as we keep the repump laser frequency detuned above the transition, the linewidth remains narrow. For the optimal detuning of the 650 I measure a power-broadened linewidth that is only $\sim$1.5x the natural linewidth, corresponding to a

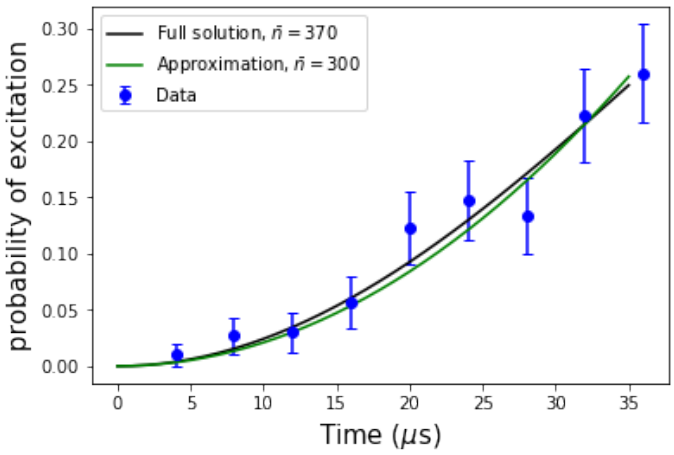

Figure 4.7: Weak excitation performed on the first blue transverse sideband of a 1762 nm transition. The ion was initially Doppler cooled. The weak excitation approximation and the full solution fit to the data quite well, but there is a 20% mismatch in $\bar{n}$ because we are getting away from the weak excitation regime.

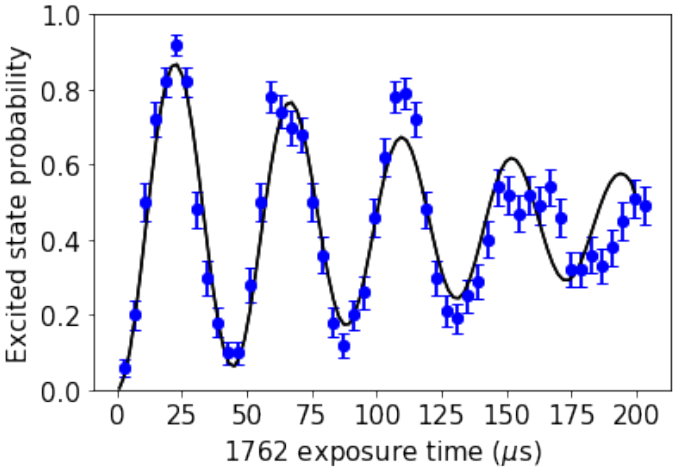

Figure 4.8: A Rabi flop which shows a decay in contrast as the number of flops increases. We fit to equation 2.42 with $n' - n = 0$. The dominant feature is a decay in the Rabi oscillations, which can normally be fit in order to extract a temperature. However our $\sim$5 kHz laser noise has an extremely similar effect, which makes it impossible to determine $\bar{n}$ unless the ion is very hot.

saturation parameter of $\sim$2.5. This should result in a Doppler cooled temperature in our radial modes of $\bar{n} \simeq 10$.

I finally discovered by varying laser powers and frequencies that the ion was cooled to a reasonable temperature with increased 650 nm laser power. While performing the initial experiments I worked with a low 650 nm power level at about twice the saturation intensity to avoid strong coherent coupling between the 650 nm and 493 nm transitions, but by poor luck the two photon coupling caused the ion to not cool efficiently there. The 650 nm and 493 nm transitions are certainly more strongly coupled at the present 650 nm power, but I found a frequency range at the present power where I could repeat the weak excitation measurement and consistently measure an $\bar{n}$ of approximately 20.

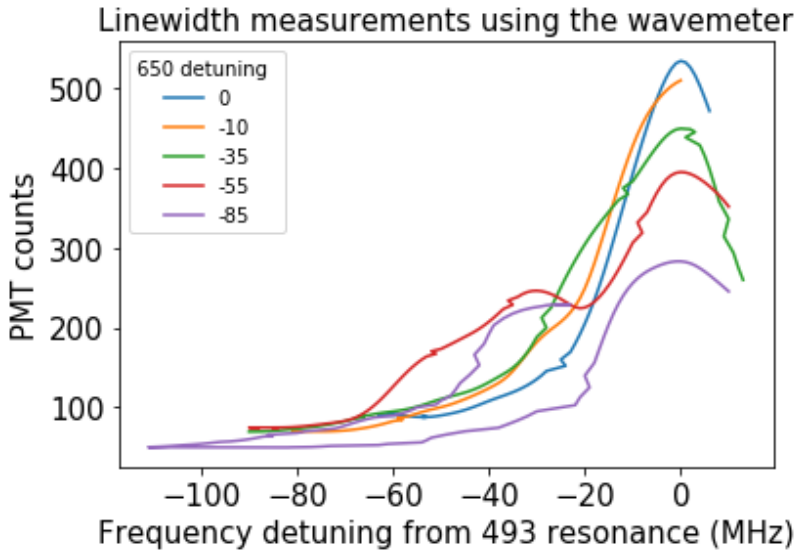

Figure 4.9: 493 nm linewidth measurements at different 650 nm detunings. The 493 nm and 650 nm lasers were locked and I trapped several ions. Any motional broadening along the radial direction should affect all ions equally, and the laser is not tightly focused, so using more ions should not change the lineshape. I recorded the PMT counts, 493 nm frequency, and time, and swept the 493 nm lock across the transition resonance. The 650 nm laser was maintained at different frequencies as plotted for the duration of each run. The large branching ratio of Ba^+gives rise to a strong coupling between the cooling and repump lasers, and the distortion of the line is obvious as the 650 nm laser frequency is decreased. The data show no broadening for the laser parameters used in the weak excitation experiment, so I was able to discount the 493 linewidth as the reason for the systematically high temperatures.

Chapter 5

MULTI SPECIES ION CHAIN TEMPERATURE MEASUREMENT

5.1 Motivation

Our experiment sprung from the MUSIQC project, which proposed using $^{138}Ba^{+}$and $^{171}Yb^{+}$ as utility and logic qubits, respectively. Ytterbium 171 is an attractive candidate as a logical qubit; it is a naturally abundant, non-radioactive, nuclear spin$-1/2$ isotope. It also has a simple atomic structure which requires only one repump laser, and a cycling transition from the ground state can be used for Doppler cooling, as well as state initialization and detection[42]. As barium has no cycling transition, initialization and detection are more difficult, but its visible cooling transitions are a boon. They make it easier to construct lasers for working with barium, increase transmissivity of its light through glass[43], and make laser alignment simpler. Perhaps most importantly for MUSIQC, the spectral separation of $Ba^{+}$and Yb^{+} transitions allow us to pursue remote entanglement and sympathetic cooling.

To sympathetically cool or remotely entangle barium and ytterbium efficiently, they must interact strongly in the trap via their Coulomb repulsion. If barium is used for remote entanglement, it is necessary to swap its entanglement onto ytterbium with local gates. The ions' mechanical coupling determines whether local entangling gates between the two species are reasonably fast. Good coupling also allows for efficient extraction of energy while sympathetically cooling. We can measure the mechanical coupling for mixed species chains by Doppler cooling a chain of Ba^{+} and Yb^{+}, and then measuring the temperature of its vibrational modes. If coupling is good, then the ytterbium ions' kinetic energy should be low; equivalently, all modes should have a low number of motional quanta.

While the normal modes of homogenous chains tend to be well coupled, I find in my data that the radial vibrational modes of mixed species chains are very poorly coupled using naive trapping parameters. I further find that significant improvements to the coupling are achievable through simple changes to the trapping potential. It is worthwhile to note that

the axial vibrational modes of mixed species chains are well coupled regardless of trapping parameters- hence, one might question why the work here is important. There are several reasons. First, cooling of the radial modes will better localize the ions, which improves gate fidelities. Further, gates that utilize radial modes have several advantages. The gate infidelity due to thermal motion of the ions is reduced for these gates by a factor between α^4 to α^6, where the aspect ratio $\alpha = \omega_{radial}/\omega_{axial} > 1$ (ω are the secular frequencies). It is also possible to perform gates in less than a single trap cycle, and these gates are easier to perform with high fidelity using the radial modes[44]. There have also been proposals for using radial gates with hundreds of ions which predict high gate fidelities[**?**]. Thus it is worthwhile to study the coupling of radial modes in these mixed species chains. I report the results of my mixed-species radial mode measurements below.

5.2 Measurement procedure, systematics

Our temperature measurement is based on weak excitation, and the procedure is similar to that of single ion weak excitation (explained in section) 4.1.1, with a few caveats. After loading a mixed species ion chain, I hold the ions overnight to allow any electric fields built up due to UV exposure to decay. Because our single channel PMT cannot distinguish signals from individual ions we instead use an EMCCD camera to record the fluorescence at the site of each ion. Reordering also becomes a nuisance in mixed species chains. If the chain reorders during the detection window, the bright and dark ions are randomized in an unknown way, which leads to crosstalk in the detection channels. It is possible to detect reordering if a bright $Ba^+$is in a previously dark site, but a shelved Ba^+ is indistinguishable from a Yb^+, so we cannot perform post-selection to rid ourselves of this noise entirely. Additionally, the same crystal configuration must be maintained for the entire experimental scan to avoid changing the normal mode spectrum, so if the chain is in the wrong order we have to fix it before we can continue our experiment. We use a simple method to reorder which works well because our trap does not lose ions easily. We turn off our cooling lasers and allow the crystal to melt, randomizing its order, and then cool it and allow the ions to recrystallize. We repeat this procedure until we have the desired order. Because of the combinatoric growth of possible configurations with ion number this method does not scale

well. Several other techniques are better suited for scaling, and have been used reorder mixed chains. In particular, the Hayasaka group in Japan working on sympathetically cooled atomic clocks modulates their Doppler cooling beams at frequencies resonant with undesired chain orderings, destabalizing them. This modulation reorders the chain to the correct configuration in only a few detection cycles, and seems extensible to larger chains[45].

Reordering has become a more troublesome systematic since the change in optical setup reduced our fluorescence collection efficiency. The required 0.5 s exposure time our camera needs to discriminate bright and dark states is long enough that the entire chain heats considerably when the refrigerant barium ions are shelved (and therefore dark). Using this longer detection window I observed that nearly every time all barium ions were shelved, the chain would reorder. To get a baseline reordering rate for comparison I blocked the 1762 laser and ran the pulse sequences. There were only a couple of reordering events in 2500 runs, (see figure 5.1), which indicates that shelving is the issue. Because of shelving-induced reordering, we cannot take data in which the ions are shelved more than about 30% of the time without systematic errors in the shelving probability of ∼20%. Setting experimental conditions such that shelving is infrequent (10-20%) reduces this systematic to ∼5% or less for 2 Ba 2 Yb chains. Thankfully, we can still perform temperature measurements that fulfill this condition with weak excitation, because the shelving probability is never too high. For larger chains the requirement that shelving should be weak will relax as at least one barium ion will remain bright most of the time and cool the chain.

The orderings that the ion chain falls into upon recooling are not completely random. The chains exhibit either instability or preferential orderings. Some causes are sensible- the ions crystallize most often in configurations which our data shows have good sympathetic cooling of ytterbium by barium. Others are less so- the precise RF power delivered to the trap plays a large role in determining the set of stable configurations. Even a 0.6% change in RF power alters the set of stable modes. To get a handle on this effect, I logged the number of runs the ions would successfully complete before reordering. I saw periods during which the ions would remain stable for hundreds of runs, and periods when they would reorder after every second or third experimental pulse sequence, with no changes apparent in 493 nm or 650 nm laser power or frequency. Worse, depending on the particular set of stable modes,

Figure 5.1: The PMT detection record of one of the barium ions in an experiment done with a mixed Ba-Yb-Ba-Yb chain. The 1762 was shuttered for the duration to test the chain stability in the dark. Each experimental run is a cross, and there are 100 runs per bin. If the ions were reordering then a Yb would have sometimes taken the Ba's place in the chain, and the record would show lower background level PMT counts of ~1000-3000. The circles indicate likely "shelving" events.

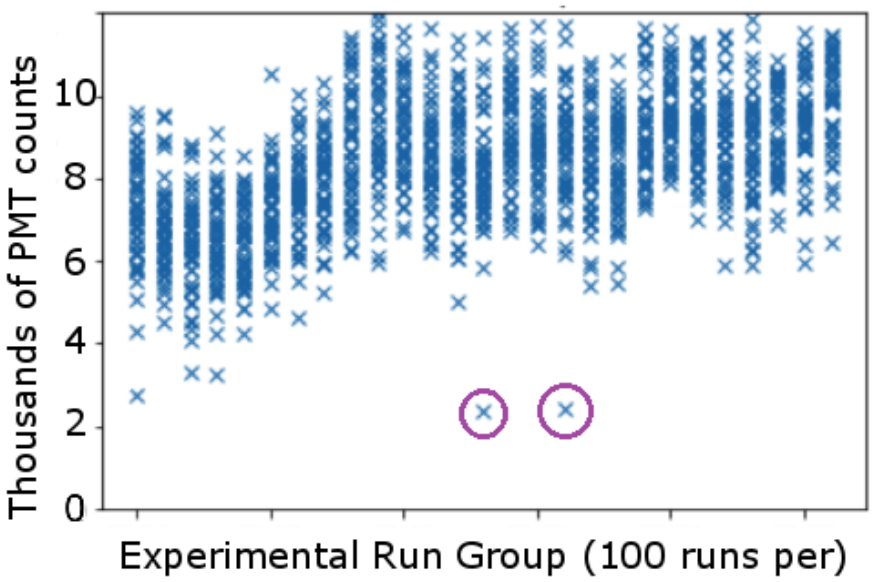

reordering to the correct configuration could take from 3-300 reorderings, which tripled or quadrupled the duration of my measurements. The longer duration makes measurements more sensitive to slow drifts of our radial secular and 1762 nm laser frequencies. If we want to improve the stability of our secular frequencies in the future, we need to improve our RF power stability there are feasible passive stabilization and active feedback techniques to do so.

5.3 Results and analysis

5.3.1 Hot chains

To perform our analysis, we must first modify equation 2.38 for use with multi ion chains. As stated previously, in a multi-ion chain the Lamb-Dicke parameter is modified as $\eta \to \eta\beta_{i,j}$, where $\beta_{i,j}$ is the eigenvector component for the ith ion in the jth mode. We excite the first blue sideband so $n' - n = 1$, and $\Omega_{n',n} = \Omega_0\eta\beta_{i,j}\sqrt{(n+1)}$. Thus we have

$$P_i(\omega_{1762}) = \sum_{i,j} \Omega_{i,0}^2 \eta^2 \beta_{i,j}^2 n \frac{\sin^2(\delta_j t/2)}{\delta_j^2}, \tag{5.1}$$

where P_i is the excitation probability for the ith ion, and $\delta_j = \omega_{1762} - \omega_j$ is the detuning of the 1762 nm laser from the jth mode secular sideband resonance. We now have sidebands for each of the different vibrational modes of the chain, so the spectrum will have many peaks. To find $\Omega_{i,0}$ for each ion we perform a Rabi flop experiment with a chain composed exclusively of barium. The equilibrium ion positions are determined only by the static coulomb repulsion, so they are the same for barium and ytterbium.

The data in figure 5.2 and table 5.1 are the first we took to characterize the temperature of these mixed species chains. There are four ions: two barium and two ytterbium. Because there also two radial directions there are eight modes total. Only four features appear in the spectrum for each ion because certain pairs of peaks overlap. To fit the data, we allow the peaks' central frequencies to float freely because otherwise our fits did not agree with the spectrum. Clearly the data show that barium was ineffective at cooling ytterbium- the ytterbium in this chain has high enough $\bar{n}$ that it is far out of the Lamb-Dicke limit for any of our lasers. (The Lamb-Dicke limit $\eta^2 n(n+1) \ll 1$ characterizes the size of the ion

Figure 5.2: Weak excitation radial sideband scan of a Ba-Ba-Yb-Yb chain and fit. The aspect ratio α of the trap here is approximately 6.5. The eight radial modes are blurred together so that only four features are visible.

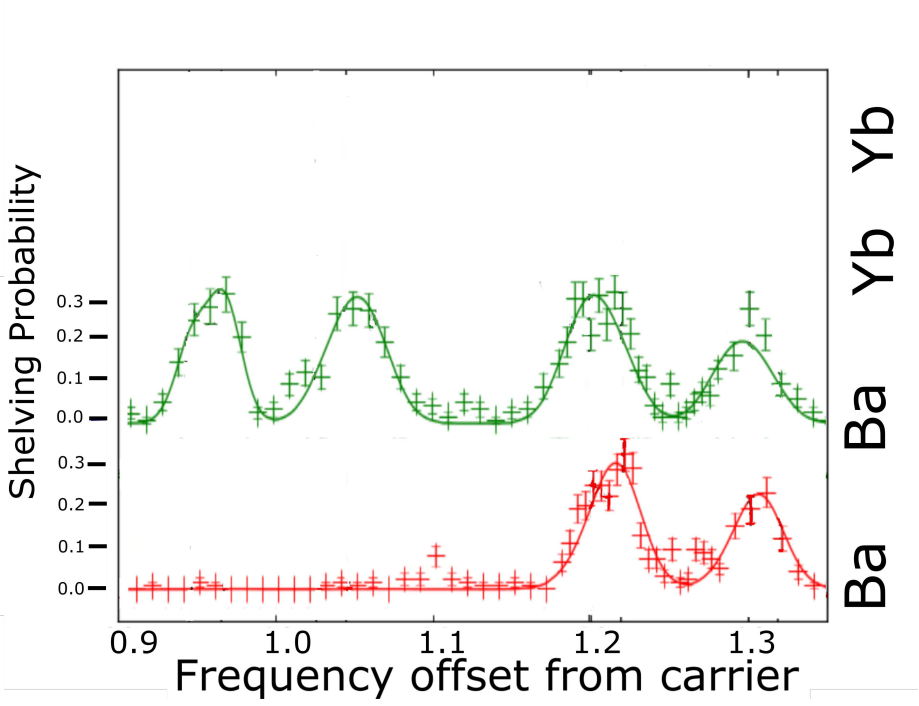

Strong Trap Ba, Ba, Yb, Yb Data

Frequency(kHz)	Barium Eigenvector Components		$\bar{n}$
1310	0.866	0.500	16
1290	-0.500	0.865	6
1200	0.865	0.501	19
1180	-0.501	0.864	10
1030	0.002	0.022	12795
1010	0.002	0.029	4968
950	0.002	0.026	7991
930	0.002	0.035	3130

Table 5.1: Eigendecomposition and occupation numbers for each mode of a Ba-Ba-Yb-Yb ion chain. The modes with small barium eigenvector components have very high occupation numbers, and the motional occupation varies strongly against the largest eigenvector component for a barium ion in the mode.

wavepacket in comparison to the excitation light.) Local entangling gates rely on the ions being within the Lamb Dicke limit to achieve acceptable fidelities for quantum computing.

5.3.2 Discovering trap conditions for cold chains

We thought that using a different ion chain configuration might better couple barium and ytterbium, so we took data for all four unique configurations. The plot for a weak excitation sideband scan of a Ba-Yb-Ba-Yb chain is shown in figure 5.3 and the associated eigendecomposition and $\bar{n}$ values are in table 5.2. They show a reduced temperature, but not one low enough so that the ytterbium ions are in the Lamb Dicke regime.

This data did push us to figure out what to change- we found a correlation between the maximum barium eigenvector component for a given mode and the measured temperature, see figure 5.4. Given that the axial modes are reasonably well coupled, I realized that motional decoupling is related to the spatial arrangement of the ions. The only knob I could

Figure 5.3: Weak excitation of a sideband spectrum of a Ba-Yb-Ba-Yb chain. The associated table 5.2 shows that this interspersed chain has lower temperatures than the Ba-Ba-Yb-Yb chain.

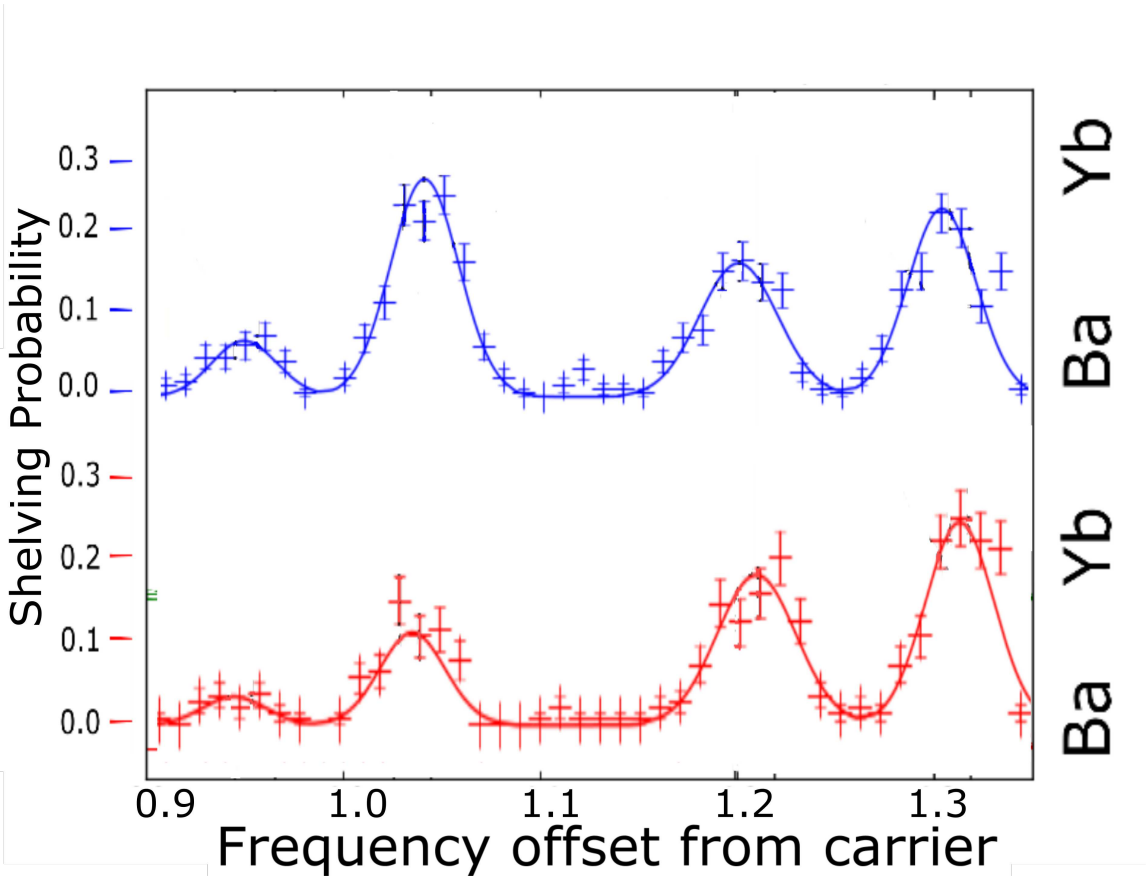

Strong Trap Ba, Yb, Ba, Yb Data

Frequency (kHz)	Barium Eigenvector Components		$\bar{n}$
1300	0.989	0.143	17
1290	-0.144	0.989	15
1200	0.988	0.148	13
1190	-0.150	0.987	11
1030	0.003	0.034	4913
1020	0.028	0.034	7427
950	0.003	0.039	490
940	0.033	0.041	1501

Table 5.2: Eigendecomposition and occupation numbers for each mode of a Ba-Yb-Ba-Yb ion chain. The size of the smaller barium eigenvector component for each mode does not change the temperature much. This can be seen because the 1.03 and 0.95 MHz modes are coupled to one barium ion more strongly than the other, while the 1.02 and 0.95 MHz modes are coupled equally to both. The $\bar{n}$ does vary strongly against the largest eigenvector component for a barium ion in the mode.

Figure 5.4: Measured average number of motional quanta versus the size of the largest barium eigenvector component in each mode. The red line is drawn to guide the eye.

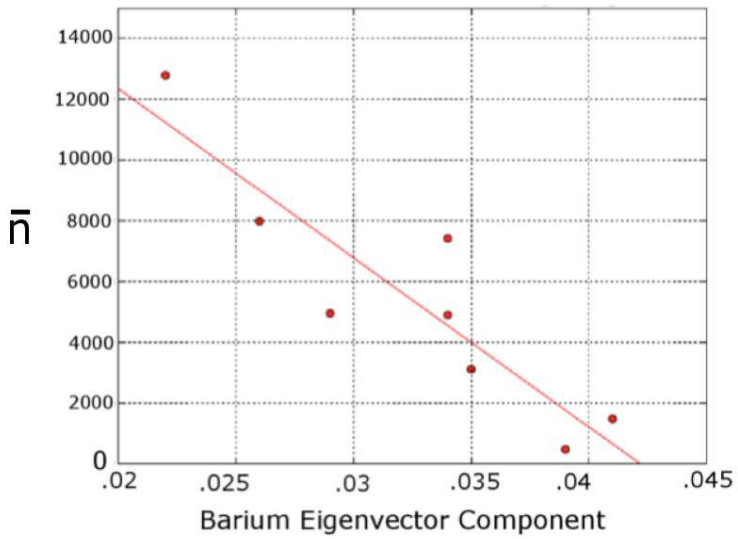

turn to change the spatial arrangement without fundamentally altering our trap system was to reduce α, the trap aspect ratio. Realizing that, I calculated the eigendecomposition as a function of the radial trap strength, and found that the small eigenvector components grow strongly as the mechanical "zig-zag" phase transition is approached, see figures 5.5 and 5.6. I discovered that the decoupling depends strongly on the aspect ratio when it is close to the critical point for a zig-zag transition.

5.3.3 Cold chain measurement & scaling to larger numbers of ions

After lowering the trap depth, I took more data. The first new dataset was taken with both sets of radial modes lowered to an aspect ratio of 4 relative to the axial, see figure 5.7 and table 5.3. Fitting its spectra was difficult because of density of peaks and the systematic noise sources I mentioned in the last section. Still, it is clear that the lower set of vibrational modes are much colder in this configuration. Despite having much larger $\beta_{i,j}$, the peaks are smaller, so much so that I needed to increase the 1762 nm exposure time to observe

Figure 5.5: Eigenvector magnitude vs trap aspect ratio for a barium ion in a Ba-Yb-Ba-Yb chain for all four modes. The larger barium eigenvector components decrease as the aspect ratio decreases, while the smaller eigenvector components increase. The aspect ratios shown are all above the critical zig-zag transition point $\alpha = 2.45 = 0.77N^{0.83}$, where N is the number of ions.

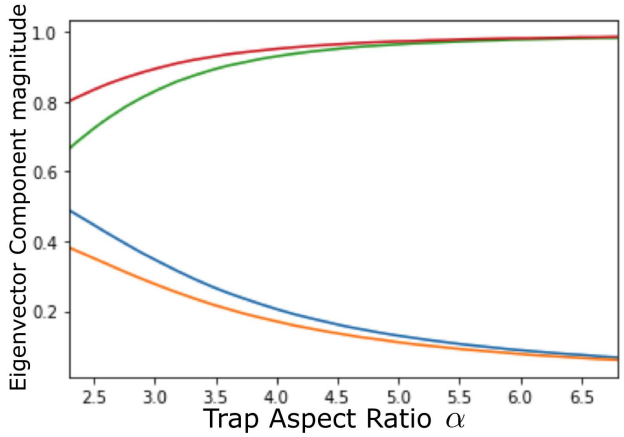

them. Even if the fit misidentified one of the peaks, the number of vibrational quanta would not change much. Given temperatures in this range, we should be able to perform useful motional gates and sympathetic cooling operations.

I wanted to take a data set that was easier to interpret, so I increased the trap strength in one transverse direction until it was at an aspect ratio of 5. This should result in one set of modes being well coupled, and the other not. The result is shown in figure 5.8; the data are in good agreement with our expectation. Note that these results agree with an intuitive picture quite nicely. The Doppler cooling force is proportional to velocity, and the barium eigenvector component reduces the size of excursions of barium for a given $\bar{n}$. A smaller eigenvector component results in a lower velocity and a weaker drag force, so if there is any non-Doppler source of heating, the ytterbium-dominant modes will have significant $\bar{n}$ before Doppler cooling becomes effective.

It is interesting to consider scaling to larger numbers of ions in the trap; eventually we will need more to build a large quantum computer. If the results from my work hold

Figure 5.6: A diagram of the phase transitions a trapped ion crystal undergoes as the radial potential is lowered. Here the radial potential in the out-of-page direction is kept strong. Barium is cyan, ytterbium is black, and equipotential surfaces are shown in red. a) At high aspect ratios the ions all lie along the trap axis. b) As the aspect ratio is lowered the ions first undergo a "zig-zag" transition with two degenerate configurations. The point at which this transition occurs can be calculated by balancing the outward force from neighboring ions with the restoring trap force. For a sufficiently small ion spacing, the outward force dominates. The axial trap determines the ion positions along the axis, so the transition is a function of both the radial and axial trap potentials. c) As the radial potential is lowered more phase transitions occur. Here the ions are shown when the trap potential is isotropic in the plane of the page.

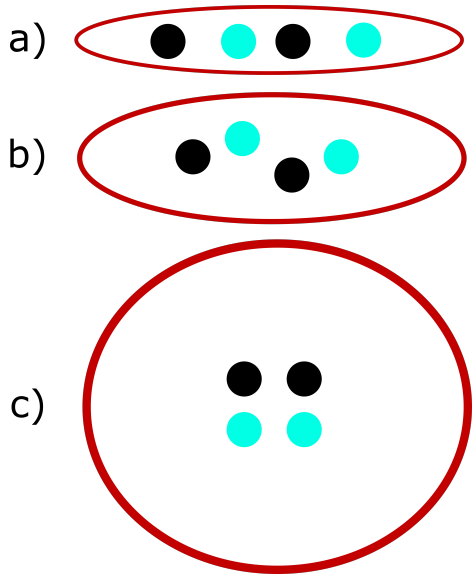

Figure 5.7: Raw data and numerically produced fit of the sideband spectrum of a Ba-Yb-Ba-Yb chain. The vertical axis is split into two separate segments for the curves shown, which correspond to the outer (red) and inner (blue) barium ions. The spectrum is also split into two sections, with the left half of the spectrum being taken with a longer excitation time. This was done so that the shelving probability would be large enough for visual representation and fitting. The associated numbers of quanta are in table 5.3. Note that the peaks will be in the same positions on both ions' spectra- they correspond to vibrational modes of the entire chain.

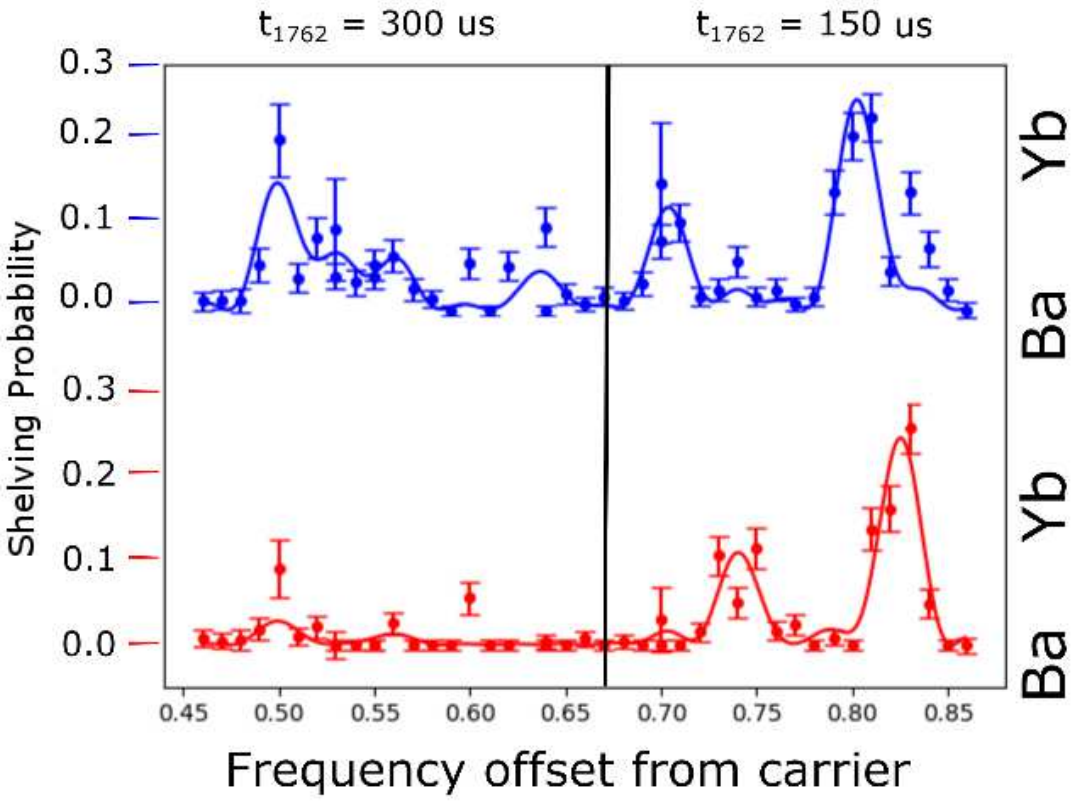

Figure 5.8: Weak excitation sideband plot for mixed Ba-Yb-Ba-Yb chain, with one radial trap axis weak and the other strong. The weak radial mode is cold, while the strong one is hot. The associated numbers of quanta are shown in table 5.4.

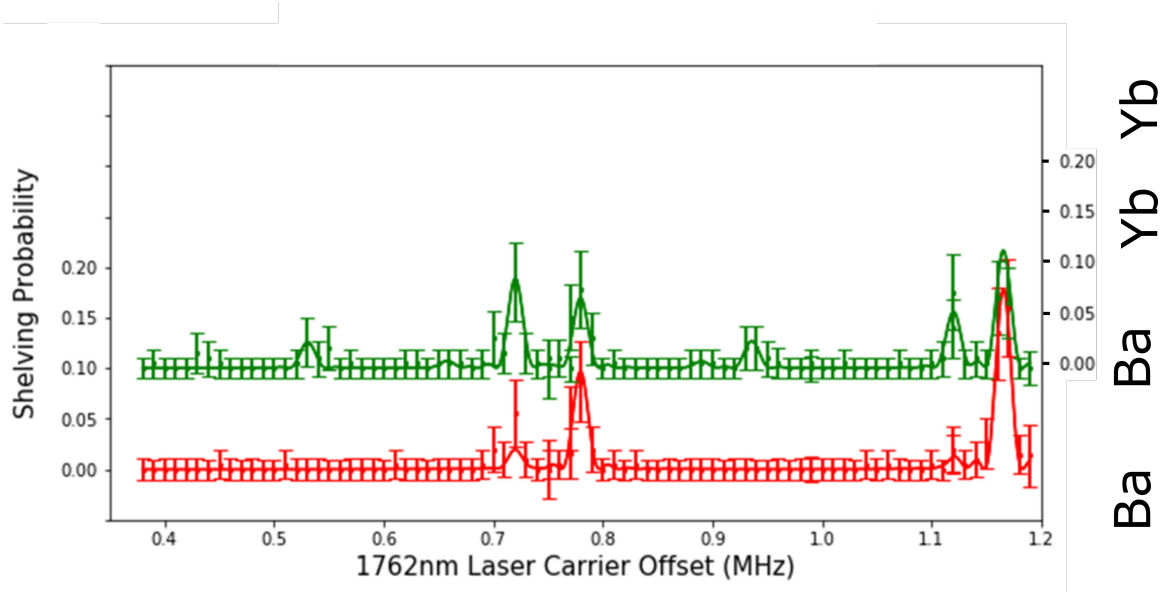

for larger numbers of ions, we should be able to scale the number of barium ions in a harmonic trap as shown in figure 5.9. There is a balance between maintaining a frequency margin away from the zig-zag transition and using a reasonable number of refrigerant ions. Preliminary calculations suggest that anharmonic traps would be better coupled radially, see figure 5.10. Anharmonic potentials are proposed for use because they lend to an even ion spacing which eases technical requirements for Raman gates. The axial modes can no longer be used for quantum gates, so the coupling factor and temperature of the radial modes would become quite crucial to the functioning of a quantum computer. It would be relatively straightforward to extend the numerical calculations to larger numbers of ions. Additionally, it appears that configurations do matter strongly for coupling of modes, see figure 5.11

Figure 5.9: Number of barium ions required to keep a barium-ytterbium chain well coupled as the total number of ions is increased. Calculation is done with barium ions interspersed throughout the chain evenly. A margin of 100 kHz is maintained from the zig-zag transition, though it should be noted that it may be important to relax this margin as the number of ions is increased. The numbers of barium ions required here are conservative, because "good coupling" is defined as being above 0.1 for the barium eigenvector component, whereas in reality that number should scale downward due to normalization.

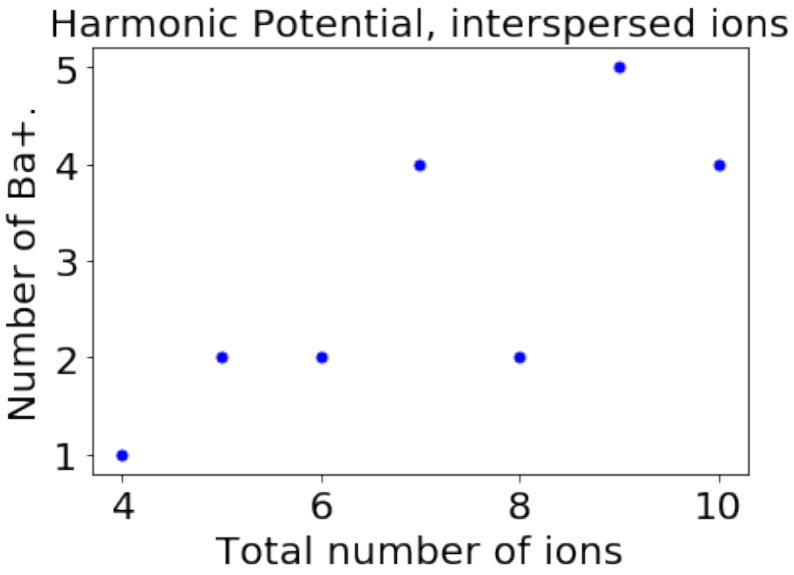

Figure 5.10: Number of interspersed barium ions required to keep a barium-ytterbium chain well coupled as the total number of ions is increased in an anharmonic trap.

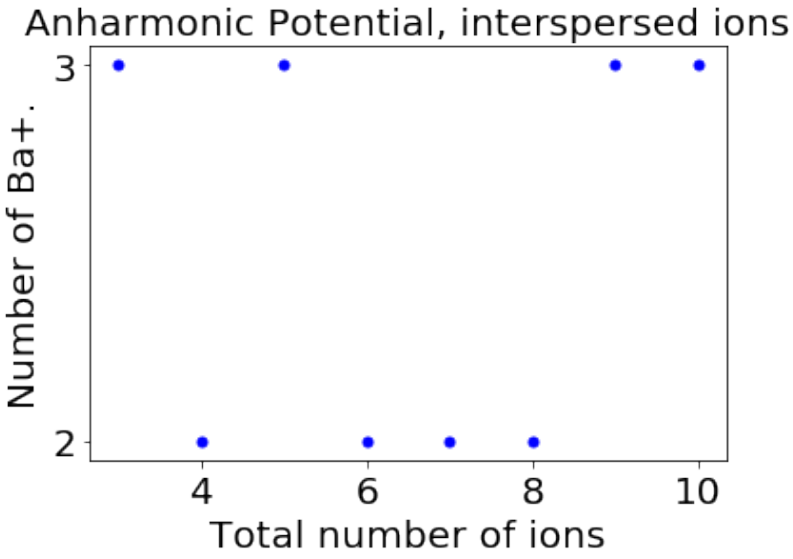

Figure 5.11: Number of barium ions required to keep a barium-ytterbium chain well coupled as the total number of ions is increased in an harmonic trap if the barium ions are at the ends of the chain.

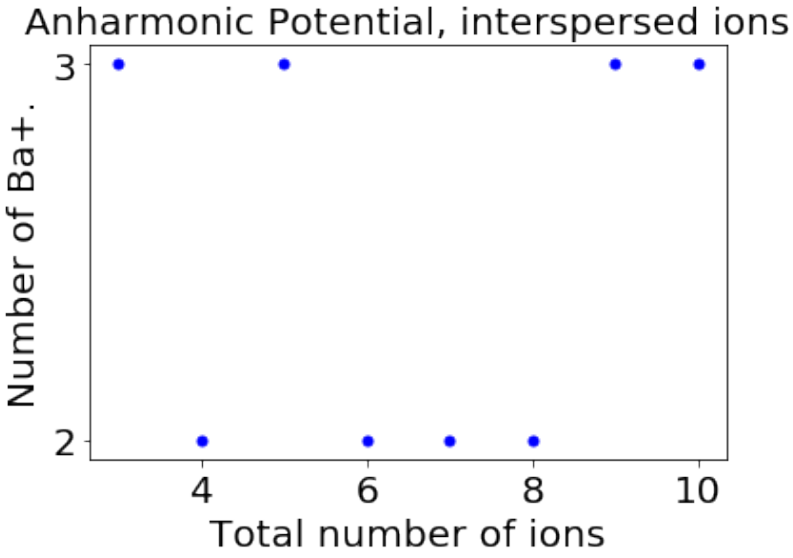

5.4 Summary & Outlook

I have built or refurbishd much of the apparatus for manipulating barium and ytterbium under the MUSIQC architecture. Significant work remains to really flesh out the possibilities of the system: only basic trapping of ytterbium has been demonstrated, and before we can control ytterbiums' atomic state we need to find a microscopy solution that will allow us to image both species. Different possibilities for solving this problem exist, including commercial optics designed for these wavelegnths, changing zoom based on the experiment, or altering the vacuum chamber geometry. Moving farther afield, performing entangling gates between barium and ytterbium should be possible, and high quality entangling gates have not yet been demonstrated between barium and ytterbium. A wide variety of phenomena exist which mixed species modifies, and we will probably discover more as we continue to work with this system. Using what capabilities the apparatus already has I have measured the efficiency of sympathetic cooling and discovered that the coupling of barium and ytterbium depends strongly on the proximity of the "zig-zag" phase transition. I have also achieved sympathetically cooled chains of moderate size well within the Doppler limit, which will allow for entangling gates between barium and ytterbium. Further, numerical calculations show that this coupling should extend to higher numbers of ions as long as the trap ratio is held close to the critical point. It remains to define what "close" means in this context, and what impact that will have on the normal modes and entangling gates.

Weak Trap Ba, Yb, Ba, Yb Data

Frequency (kHz)	Barium Eigenvector Components	$\bar{n}$
816	0.83	43
755	0.85	18
632	0.13	28
564	-0.15	25
734	0.85	28
667	0.82	13
566	0.18	23
490	0.19	35

Table 5.3: Eigendecomposition and occupation numbers for each mode of a Ba-Yb-Ba-Yb ion chain with a reduced aspect ratio for both radial mdoes. All occupation numbers are within a few times the Doppler limit for barium.

Ba, Yb, Ba, Yb Radial Mode Data

Frequency (kHz)	Barium Eigenvector Components	$\bar{n}$
1180	0.86	60
1138	0.86	9
926	0.06	825
874	-0.08	112
783	0.85	58
720	0.83	22
602	0.15	10
533	0.16	23

Table 5.4: Eigendecomposition and occupation numbers for each mode of a Ba-Yb-Ba-Yb ion chain, with varied trap strength. The ytterbium mode temperature begins to grow very strongly below an eigenvector component size of about 0.09.

BIBLIOGRAPHY

[1] Peter W Shor. Algorithms for quantum computation: Discrete logarithms and factoring. In *Foundations of Computer Science, 1994 Proceedings., 35th Annual Symposium on*, pages 124–134. Ieee, 1994.

[2] C. Monroe, R. Raussendorf, A. Ruthven, K. R. Brown, P. Maunz, L.-M. Duan, and J. Kim. Large-scale modular quantum-computer architecture with atomic memory and photonic interconnects. *Phys. Rev. A*, 89:022317, Feb 2014.

[3] Christoph Kloeffel and Daniel Loss. Prospects for spin-based quantum computing in quantum dots. *Annual Review of Condensed Matter Physics*, 4(1):51–81, 2013.

[4] M. H. Devoret and R. J. Schoelkopf. Superconducting circuits for quantum information: An outlook. *Science*, 339(6124):1169–1174, 2013.

[5] M. Saffman, T. G. Walker, and K. Mølmer. Quantum information with rydberg atoms. *Rev. Mod. Phys.*, 82:2313–2363, Aug 2010.

[6] Pieter Kok, W. J. Munro, Kae Nemoto, T. C. Ralph, Jonathan P. Dowling, and G. J. Milburn. Linear optical quantum computing with photonic qubits. *Reviews of Modern Physics*, 79(1):135–174, jan 2007.

[7] Dorit Aharonov, Wim Van Dam, Julia Kempe, Zeph Landau, Seth Lloyd, and Oded Regev. Adiabatic quantum computation is equivalent to standard quantum computation. *SIAM review*, 50(4):755–787, 2008.

[8] Richard Jozsa. An introduction to measurement based quantum computation. *NATO Science Series, III: Computer and Systems Sciences. Quantum Information Processing-From Theory to Experiment*, 199:137–158, 2006.

[9] Rami Barends, Julian Kelly, Anthony Megrant, Andrzej Veitia, Daniel Sank, Evan Jeffrey, Ted C White, Josh Mutus, Austin G Fowler, Brooks Campbell, et al. Superconducting quantum circuits at the surface code threshold for fault tolerance. *Nature*, 508(7497):500–503, 2014.

[10] Dietrich Leibfried, Brian DeMarco, Volker Meyer, David Lucas, et al. Experimental demonstration of a robust, high-fidelity geometric two ion-qubit phase gate. *Nature*, 422(6930):412, 2003.

[11] Jan Benhelm, Gerhard Kirchmair, Christian F Roos, and Rainer Blatt. Towards fault-tolerant quantum computing with trapped ions. *arXiv preprint arXiv:0803.2798*, 2008.

[12] R. Barends, J. Kelly, A. Megrant, A. Veitia, D. Sank, E. Jeffrey, T. C. White, J. Mutus, A. G. Fowler, B. Campbell, Y. Chen, Z. Chen, B. Chiaro, A. Dunsworth, C. Neill, P. O'Malley, P. Roushan, A. Vainsencher, J. Wenner, A. N. Korotkov, A. N. Cleland, and John M. Martinis. Superconducting quantum circuits at the surface code threshold for fault tolerance. *Nature*, 508(7497):500–503, 2014.

[13] Daniel Alsina and José Ignacio Latorre. Experimental test of mermin inequalities on a five-qubit quantum computer. *Physical Review A*, 94(1):012314, 2016.

[14] Simon J Devitt. Performing quantum computing experiments in the cloud. *Physical Review A*, 94(3):032329, 2016.

[15] Ryan Babbush. Towards an exact (quantum) description of chemistry. web, July 2016.

[16] David J Reilly. Engineering the quantum-classical interface of solid-state qubits. 1:15011, oct 2015.

[17] Norbert M. Linke, Dmitri Maslov, Martin Roetteler, Shantanu Debnath, Caroline Figgatt, Kevin A. Landsman, Kenneth Wright, and Christopher Monroe. Experimental comparison of two quantum computing architectures. *Proceedings of the National Academy of Sciences*, 114(13):3305–3310, 2017.

[18] David P. DiVincenzo. The physical implementation of quantum computation. *Fortschritte der Physik*, 48(9-11):771–783, 2000.

[19] C Monroe, R Raussendorf, A Ruthven, KR Brown, P Maunz, L-M Duan, and J Kim. Large-scale modular quantum-computer architecture with atomic memory and photonic interconnects. *Physical Review A*, 89(2):022317, 2014.

[20] U. Warring, C. Ospelkaus, Y. Colombe, R. Jördens, D. Leibfried, and D. J. Wineland. Individual-ion addressing with microwave field gradients. *Phys. Rev. Lett.*, 110:173002, Apr 2013.

[21] R. Srinivas S.C. Burd A.C. Wilson D. Leibfreid D.J. Wineland D.T.C. Allcock, D.H. Slichter. Trapped-ion quantum logic with near-field microwave-driven gates. In *North American Conference on Trapped Ions*, 2017.

[22] J. I. Cirac and P. Zoller. Quantum computations with cold trapped ions. *Phys. Rev. Lett.*, 74:4091–4094, May 1995.

[23] D. N. Matsukevich, P. Maunz, D. L. Moehring, S. Olmschenk, and C. Monroe. Bell inequality violation with two remote atomic qubits. *Phys. Rev. Lett.*, 100:150404, Apr 2008.

[24] S. Olmschenk, D. N. Matsukevich, P. Maunz, D. Hayes, L.-M. Duan, and C. Monroe. Quantum Teleportation Between Distant Matter Qubits. *Science*, 323(5913), 2009.

[25] K. Blaum, Yu. N. Novikov, and G. Werth. Penning traps as a versatile tool for precise experiments in fundamental physics. *Contemporary Physics*, 51(2):149–175, 2010.

[26] Justin G. Bohnet, Brian C. Sawyer, Joseph W. Britton, Michael L. Wall, Ana Maria Rey, Michael Foss-Feig, and John J. Bollinger. Quantum spin dynamics and entanglement generation with hundreds of trapped ions. *Science*, 352(6291), 2016.

[27] Wolfgang Paul. Electromagnetic traps for charged and neutral particles. *Rev. Mod. Phys.*, 62:531–540, Jul 1990.

[28] J. Gurell, E. Biémont, K. Blagoev, V. Fivet, P. Lundin, S. Mannervik, L.-O. Norlin, P. Quinet, D. Rostohar, P. Royen, and P. Schef. Laser-probing measurements and calculations of lifetimes of the $5d\,^2d_{32}$ and $5d\,^2d_{52}$ metastable levels in Ba *ii*. *Phys. Rev. A*, 75:052506, May 2007.

[29] Hilmar Oberst. *Resonance Fluorescence of single Barium ions*. PhD thesis, Innsbruck, 1999.

[30] K-A Brickman Soderberg and C Monroe. Phonon-mediated entanglement for trapped ion quantum computing. *Reports on Progress in Physics*, 73(3):036401, 2010.

[31] Daniel FV James. Quantum dynamics of cold trapped ions with application to quantum computation. *Applied Physics B: Lasers and Optics*, 66(2):181–190, 1998.

[32] John Wright. *Mixed Species Ion Chains for Scalable Quantum Computation*. PhD thesis, University of Washington, 2015.

[33] AV Steele, LR Churchill, PF Griffin, and MS Chapman. Photoionization and photoelectric loading of barium ion traps. *Physical Review A*, 75(5):053404, 2007.

[34] Atam Prakash Dhawan, Rangaraj M. Rangayyan, and Richard Gordon. Image restoration by wiener deconvolution in limited-view computed tomography. *Appl. Opt.*, 24(23):4013–4020, Dec 1985.

[35] G. Janik, W. Nagourney, and H. Dehmelt. Doppler-free optical spectroscopy on the ba+ mono-ion oscillator. *J. Opt. Soc. Am. B*, 2(8):1251–1257, Aug 1985.

[36] L Sun, L Zhang, H J Yu, L Guo, J L Ma, J Zhang, W Hou, X C Lin, and J M Li. 880 nm LD pumped passive mode-locked TEM00 Nd:YVO_4 laser based on sesam. *Laser Physics Letters*, 7(10):711, 2010.

[37] Herman A Haus. Theory of mode locking with a fast saturable absorber. *Journal of Applied Physics*, 46(3049), 1975.

[38] J. J. García-Ripoll, P. Zoller, and J. I. Cirac. Speed optimized two-qubit gates with laser coherent control techniques for ion trap quantum computing. *Phys. Rev. Lett.*, 91:157901, Oct 2003.

[39] Matthew Dietrich. *Barium Ions for Quantum Computation*. PhD thesis, University of Washington, 2009.

[40] T. Noel, M. R. Dietrich, N. Kurz, G. Shu, J. Wright, and B. B. Blinov. Adiabatic passage in the presence of noise. *Phys. Rev. A*, 85:023401, Feb 2012.

[41] D. J. Berkeland, J. D. Miller, J. C. Bergquist, W. M. Itano, and D. J. Wineland. Minimization of ion micromotion in a paul trap. *Journal of Applied Physics*, 83(10):5025–5033, 1998.

[42] S Olmschenk, KC Younge, DL Moehring, DN Matsukevich, P Maunz, and C Monroe. Manipulation and detection of a trapped yb+ hyperfine qubit. *Physical Review A*, 76(5):052314, 2007.

[43] J. E. Sansonetti and W. C. Martin. Handbook of basic atomic spectroscopic data. *Journal of Physical and Chemical Reference Data*, 34(4):1559–2259, 2005.

[44] J. Mizrahi, B. Neyenhuis, K. G. Johnson, W. C. Campbell, C. Senko, D. Hayes, and C. Monroe. Quantum control of qubits and atomic motion using ultrafast laser pulses. *Applied Physics B*, 114(1-2):45–61, jan 2014.

[45] K Hayasaka. Synthesis of two-species ion chains for a new optical frequency standard with an indium ion. *Applied Physics B*, 107(4):965–970, 2012.

[46] K. Hayasaka. Synthesis of two-species ion chains for a new optical frequency standard with an indium ion. *Applied Physics B*, 107(4):965–970, 2012.

[47] Dayou Yang, Gouri Shankar Giri, Michael Johanning, Christof Wunderlich, Peter Zoller, and Philipp Hauke. Analog quantum simulation of $(1+1)$-dimensional lattice qed with trapped ions. *Phys. Rev. A*, 94:052321, Nov 2016.

[48] Rami Barends, Julian Kelly, Anthony Megrant, Andrzej Veitia, Daniel Sank, Evan Jeffrey, Ted C White, Josh Mutus, Austin G Fowler, Brooks Campbell, et al. Superconducting quantum circuits at the surface code threshold for fault tolerance. *Nature*, 508(7497):500–503, 2014.

[49] Dietrich Leibfried, Brian DeMarco, Volker Meyer, David Lucas, et al. Experimental demonstration of a robust, high-fidelity geometric two ion-qubit phase gate. *Nature*, 422(6930):412, 2003.

[50] Christopher J Foot. *Atomic physics*, volume 7. Oxford University Press, 2005.

[51] Hans Dehmelt. A single atomic particle forever floating at rest in free space: New value for electron radius. *Physica Scripta*, 1988(T22):102, 1988.

[52] K. J. Ross and B. Sonntag. High temperature metal atom beam sources. *Review of Scientific Instruments*, 66(9):4409–4433, 1995.

[53] P. Robrish. Single-mode electro-optically tuned nd:yvo4 laser. *Opt. Lett.*, 19(11):813–815, Jun 1994.

[54] D. J. Heinzen and D. J. Wineland. Quantum-limited cooling and detection of radio-frequency oscillations by laser-cooled ions. *Phys. Rev. A*, 42:2977–2994, Sep 1990.

[55] Carolyn Auchter, Chen-Kuan Chou, Thomas W. Noel, and Boris B. Blinov. Ion-photon entanglement and bell inequality violation with $^{138}Ba^{+}$. *J. Opt. Soc. Am. B*, 31(7):1568–1572, Jul 2014.

[56] R. D. Graham, S.-P. Chen, T. Sakrejda, J. Wright, Z. Zhou, and B. B. Blinov. A system for trapping barium ions in a microfabricated surface trap. *AIP Advances*, 4(5), 2014.

[57] Gang Shu, Chen-Kuan Chou, Nathan Kurz, Matthew R. Dietrich, and Boris B. Blinov. Efficient fluorescence collection and ion imaging with the "tack" ion trap. *J. Opt. Soc. Am. B*, 28(12):2865–2870, Dec 2011.

[58] M. R. Dietrich, N. Kurz, T. Noel, G. Shu, and B. B. Blinov. Hyperfine and optical barium ion qubits. *Phys. Rev. A*, 81:052328, May 2010.

[59] R. Islam, C. Senko, W. C. Campbell, S. Korenblit, J. Smith, A. Lee, E. E. Edwards, C.-C. J. Wang, J. K. Freericks, and C. Monroe. Emergence and frustration of magnetism with variable-range interactions in a quantum simulator. *Science*, 340(6132):583–587, 2013.

[60] Waseem S. Bakr, Jonathon I. Gillen, Amy Peng, Simon Folling, and Markus Greiner. A quantum gas microscope for detecting single atoms in a Hubbard-regime optical lattice. *Nature*, 462(7269):74–77, Nov 2009.

[61] Thomas Monz, Philipp Schindler, Julio T. Barreiro, Michael Chwalla, Daniel Nigg, William A. Coish, Maximilian Harlander, Wolfgang Hänsel, Markus Hennrich, and Rainer Blatt. 14-qubit entanglement: Creation and coherence. *Phys. Rev. Lett.*, 106:130506, Mar 2011.

[62] S. Olmschenk, K. C. Younge, D. L. Moehring, D. N. Matsukevich, P. Maunz, and C. Monroe. Manipulation and detection of a trapped Yb^+ hyperfine qubit. *Phys. Rev. A*, 76:052314, Nov 2007.

[63] Emily Mount, So-Young Baek, Matthew Blain, Daniel Stick, Daniel Gaultney, Stephen Crain, Rachel Noek, Taehyun Kim, Peter Maunz, and Jungsang Kim. Single qubit manipulation in a microfabricated surface electrode ion trap. *New Journal of Physics*, 15(9):093018, 2013.

[64] Rachel Noek, Geert Vrijsen, Daniel Gaultney, Emily Mount, Taehyun Kim, Peter Maunz, and Jungsang Kim. High speed, high fidelity detection of an atomic hyperfine qubit. *Opt. Lett.*, 38(22):4735–4738, Nov 2013.

[65] Anders Sørensen and Klaus Mølmer. Entanglement and quantum computation with ions in thermal motion. *Phys. Rev. A*, 62:022311, Jul 2000.

[66] J. Mizrahi, C. Senko, B. Neyenhuis, K. G. Johnson, W. C. Campbell, C. W. S. Conover, and C. Monroe. Ultrafast spin-motion entanglement and interferometry with a single atom. *Phys. Rev. Lett.*, 110:203001, May 2013.

[67] Christopher M. Dawson and Michael A. Nielsen. The Solovay-Kitaev algorithm. *Quantum Info. Comput.*, 6(1):81–95, January 2006.

[68] K. R. Brown, A. C. Wilson, Y. Colombe, C. Ospelkaus, A. M. Meier, E. Knill, D. Leibfried, and D. J. Wineland. Single-qubit-gate error below 10^{-4} in a trapped ion. *Phys. Rev. A*, 84:030303, Sep 2011.

[69] Peter W. Shor. Scheme for reducing decoherence in quantum computer memory. *Phys. Rev. A*, 52:R2493–R2496, Oct 1995.

[70] Daniel K. L. Oi, Simon J. Devitt, and Lloyd C. L. Hollenberg. Scalable error correction in distributed ion trap computers. *Phys. Rev. A*, 74:052313, Nov 2006.

[71] Lin, G.-D., Zhu, S.-L., Islam, R., Kim, K., Chang, M.-S., Korenblit, S., Monroe, C., and Duan, L.-M. Large-scale quantum computation in an anharmonic linear ion trap. *EPL*, 86(6):60004, 2009.

[72] D. L. Moehring, M. J. Madsen, B. B. Blinov, and C. Monroe. Experimental bell inequality violation with an atom and a photon. *Phys. Rev. Lett.*, 93:090410, Aug 2004.

[73] A. Stute, B. Casabone, P. Schindler, T. Monz, P. O. Schmidt, B. Brandstatter, T. E. Northup, and R. Blatt. Tunable ion-photon entanglement in an optical cavity. *Nature*, 485(7399):482–485, May 2012.

[74] J. D. Sterk, L. Luo, T. A. Manning, P. Maunz, and C. Monroe. Photon collection from a trapped ion-cavity system. *Phys. Rev. A*, 85:062308, Jun 2012.

[75] Craig R. Clark, Chin-wen Chou, R. Ellis, A. Jeff Hunker, Shanalyn A. Kemme, Peter Maunz, Boyan Tabakov, Chris Tigges, and Daniel L. Stick. Characterization of fluorescence collection optics integrated with a microfabricated surface electrode ion trap. *Phys. Rev. Applied*, 1:024004, Mar 2014.

[76] D L Moehring, C Highstrete, D Stick, K M Fortier, R Haltli, C Tigges, and M G Blain. Design, fabrication and experimental demonstration of junction surface ion traps. *New Journal of Physics*, 13(7):075018, 2011.

[77] R. Bowler, J. Gaebler, Y. Lin, T. R. Tan, D. Hanneke, J. D. Jost, J. P. Home, D. Leibfried, and D. J. Wineland. Coherent diabatic ion transport and separation in a multizone trap array. *Phys. Rev. Lett.*, 109:080502, Aug 2012.

[78] A. Olkhovets, P. Phanaphat, C. Nuzman, D.J. Shin, C. Lichtenwalner, M. Kozhevnikov, and J. Kim. Performance of an optical switch based on 3-d mems crossconnect. *Photonics Technology Letters, IEEE*, 16(3):780–782, March 2004.

[79] Y. Lin, J. P. Gaebler, T. R. Tan, R. Bowler, J. D. Jost, D. Leibfried, and D. J. Wineland. Sympathetic electromagnetically-induced-transparency laser cooling of motional modes in an ion chain. *Phys. Rev. Lett.*, 110:153002, Apr 2013.

[80] C. F. Roos, D. Leibfried, A. Mundt, F. Schmidt-Kaler, J. Eschner, and R. Blatt. Experimental demonstration of ground state laser cooling with electromagnetically induced transparency. *Phys. Rev. Lett.*, 85:5547–5550, Dec 2000.

[81] Brian C. Sawyer, Joseph W. Britton, Adam C. Keith, C.-C. Joseph Wang, James K. Freericks, Hermann Uys, Michael J. Biercuk, and John J. Bollinger. Spectroscopy and thermometry of drumhead modes in a mesoscopic trapped-ion crystal using entanglement. *Phys. Rev. Lett.*, 108:213003, May 2012.

[82] Joseph W. Britton, Brian C. Sawyer, Adam C. Keith, C..-C. Joseph Wang, James K. Freericks, Hermann Uys, Michael J. Biercuk, and John J. Bollinger. Engineered two-dimensional ising interactions in a trapped-ion quantum simulator with hundreds of spins. *Nature*, 484(7395):489–492, 2012.

[83] K. Blaum, Yu. N. Novikov, and G. Werth. Penning traps as a versatile tool for precise experiments in fundamental physics. *Contemporary Physics*, 51(2):149–175, 2010.

[84] J.D. Siverns, L.R. Simkins, S. Weidt, and W.K. Hensinger. On the application of radio frequency voltages to ion traps via helical resonators. *Applied Physics B*, 107(4):921–934, 2012.

[85] Kenneth Wright, Jason M Amini, Daniel L Faircloth, Curtis Volin, S Charles Doret, Harley Hayden, C-S Pai, David W Landgren, Douglas Denison, Tyler Killian, Richart E Slusher, and Alexa W Harter. Reliable transport through a microfabricated X-junction surface-electrode ion trap. *New Journal of Physics*, 15(3):033004, 2013.

[86] D.T.C. Allcock, T.P. Harty, H.A. Janacek, N.M. Linke, C.J. Ballance, A.M. Steane, D.M. Lucas, Jr. Jarecki, R.L., S.D. Habermehl, M.G. Blain, D. Stick, and D.L. Moehring. Heating rate and electrode charging measurements in a scalable, microfabricated, surface-electrode ion trap. *Applied Physics B*, 107(4):913–919, 2012.

[87] N Daniilidis, S Narayanan, S A Möller, R Clark, T E Lee, P J Leek, A Wallraff, St Schulz, F Schmidt-Kaler, and H Häffner. Fabrication and heating rate study of microscopic surface electrode ion traps. *New Journal of Physics*, 13(1):013032, 2011.

[88] A. Härter, A. Krükow, A. Brunner, and J. Hecker Denschlag. Long-term drifts of stray electric fields in a paul trap. *Applied Physics B*, 114(1-2):275–281, 2014.

[89] Hans Karlsson and Ulf Litzén. Revised Ba I and Ba II wavelengths and energy levels derived by fourier transform spectroscopy. *Physica Scripta*, 60(4):321, 1999.

[90] M. Roberts, P. Taylor, G. P. Barwood, W. R. C. Rowley, and P. Gill. Observation of the $^2S_{1/2}$–$^2F_{7/2}$ electric octupole transition in a single $^{171}Yb^+$ ion. *Phys. Rev. A*, 62:020501, Jul 2000.

[91] Brookhaven National Laboratory National Nuclear Data Center. Nudat (nuclear structure and decay data), March 18, 2008 2008.

[92] Jürgen Eschner, Giovanna Morigi, Ferdinand Schmidt-Kaler, and Rainer Blatt. Laser cooling of trapped ions. *J. Opt. Soc. Am. B*, 20(5):1003–1015, May 2003.

[93] Wayne M. Itano and D. J. Wineland. Laser cooling of ions stored in harmonic and penning traps. *Phys. Rev. A*, 25:35–54, Jan 1982.

[94] R. B. Blakestad, C. Ospelkaus, A. P. VanDevender, J. M. Amini, J. Britton, D. Leibfried, and D. J. Wineland. High-fidelity transport of trapped-ion qubits through an X-junction trap array. *Phys. Rev. Lett.*, 102:153002, Apr 2009.

[95] R. B Blakestad, C. Ospelkaus, A. P VanDevender, J. H Wesenberg, M. J Biercuk, D. Leibfried, and D. J Wineland. Near-ground-state transport of trapped-ion qubits through a multidimensional array. *Phys. Rev. A*, 84:032314, Sep 2011.

[96] Jaroslaw Labaziewicz, Yufei Ge, Paul Antohi, David Leibrandt, Kenneth R. Brown, and Isaac L. Chuang. Suppression of heating rates in cryogenic surface-electrode ion traps. *Phys. Rev. Lett.*, 100:013001, Jan 2008.

[97] J. Chiaverini and J. M. Sage. Insensitivity of the rate of ion motional heating to trap-electrode material over a large temperature range. *Phys. Rev. A*, 89:012318, Jan 2014.

[98] Michael Niedermayr, Kirill Lakhmanskiy, Muir Kumph, Stefan Partel, Jonannes Edlinger, Michael Brownnutt, and Rainer Blatt. Cryogenic surface ion trap based on intrinsic silicon. *New Journal of Physics*, 16(11):113068, 2014.

[99] G. Shu, G. Vittorini, A. Buikema, C. S. Nichols, C. Volin, D. Stick, and Kenneth R. Brown. Heating rates and ion-motion control in a Y-junction surface-electrode trap. *Phys. Rev. A*, 89:062308, Jun 2014.

[100] Y. Ibaraki, U. Tanaka, and S. Urabe. Detection of parametric resonance of trapped ions for micromotion compensation. *Applied Physics B*, 105(2):219–223, 2011.

[101] A. Safavi-Naini, P. Rabl, P. F. Weck, and H. R. Sadeghpour. Microscopic model of electric-field-noise heating in ion traps. *Phys. Rev. A*, 84:023412, Aug 2011.

[102] D. A. Hite, Y. Colombe, A. C. Wilson, K. R. Brown, U. Warring, R. Jördens, J. D. Jost, K. S. McKay, D. P. Pappas, D. Leibfried, and D. J. Wineland. 100-fold reduction of electric-field noise in an ion trap cleaned with *In Situ* argon-ion-beam bombardment. *Phys. Rev. Lett.*, 109:103001, Sep 2012.

[103] N. Daniilidis, S. Gerber, G. Bolloten, M. Ramm, A. Ransford, E. Ulin-Avila, I. Talukdar, and H. Häffner. Surface noise analysis using a single-ion sensor. *Phys. Rev. B*, 89:245435, Jun 2014.

[104] J P Home, D Hanneke, J D Jost, D Leibfried, and D J Wineland. Normal modes of trapped ions in the presence of anharmonic trap potentials. *New Journal of Physics*, 13(7):073026, 2011.

[105] Shannon X. Wang, Jaroslaw Labaziewicz, Yufei Ge, Ruth Shewmon, and Isaac L. Chuang. Individual addressing of ions using magnetic field gradients in a surface-electrode ion trap. *Applied Physics Letters*, 94(9):–, 2009.

[106] D. Hayes, S. M. Clark, S. Debnath, D. Hucul, I. V. Inlek, K. W. Lee, Q. Quraishi, and C. Monroe. Coherent error suppression in multiqubit entangling gates. *Phys. Rev. Lett.*, 109:020503, Jul 2012.

[107] D. Hayes, D. N. Matsukevich, P. Maunz, D. Hucul, Q. Quraishi, S. Olmschenk, W. Campbell, J. Mizrahi, C. Senko, and C. Monroe. Entanglement of atomic qubits using an optical frequency comb. *Phys. Rev. Lett.*, 104:140501, Apr 2010.

[108] W. C. Campbell, J. Mizrahi, Q. Quraishi, C. Senko, D. Hayes, D. Hucul, D. N. Matsukevich, P. Maunz, and C. Monroe. Ultrafast gates for single atomic qubits. *Phys. Rev. Lett.*, 105:090502, Aug 2010.

[109] Adrian Schlatter, S. C. Zeller, R. Grange, R. Paschotta, and U. Keller. Pulse-energy dynamics of passively mode-locked solid-state lasers above the q-switching threshold. *J. Opt. Soc. Am. B*, 21(8):1469–1478, Aug 2004.

[110] John David Jackson. *Classical Electrodynamics*. John Wiley and Sons, Hoboken, NJ, 1999.

[111] Christopher J. Foot. *Atomic Physics*. Oxford University Press, New York, NY, 2005.

[112] J. J. Sakurai. *Modern Quantum Mechanics*. Addison-Wesley, 1994.

[113] Shmuel Fishman, Gabriele De Chiara, Tommaso Calarco, and Giovanna Morigi. Structural phase transitions in low-dimensional ion crystals. *Physical Review B*, 77(6):064111, feb 2008.

[114] C. Monroe and J. Kim. Scaling the Ion Trap Quantum Processor. *Science*, 339(6124), 2013.